POLITECNICO DI TORINO

Corso di Laurea in Ingegneria Aerospaziale

Anno Accademico 2021/2022

Tesi di Laurea Magistrale

Development of an experimental test bench for the validation of prognostic algorithms for electromechanical actuators

Relatori:
Paolo MAGGIORE
Matteo Davide Lorenzo DALLA VEDOVA

Correlatore:
Pier Carlo BERRI

Candidato:
Matteo BERTONE

Abstract

In the recent times, the aerospace industry is moving toward the development of more electric aircraft. This shift involves a transition from an hydraulic to an electric type of actuation. Conversion that promises to reduce the overall weight of the aircraft while increasing the efficiency of the system. However, the use of electric-type actuators called EMAs is currently limited to non-safety critical functions given the still basic insight into the behavior of these systems.

To compensate for the lack of confidence in the EMAs systems, the use of prognostic techniques has found ample opportunity. The model-based approach described in the following pages is intended to reproduce the behavior of an actuation characterized by reaction times that fall somewhere between those of a primary and a secondary flight control system. The use of a model makes it possible to reproduce the performance of the system with high accuracy but renders necessary the verification of its fidelity to the actual system.

To perform model verification, a test bench was therefore assembled, the general architecture of which can be divided into two segments: the one representing the EMA system and another one delegated to the generation of resistive torques. The control architecture selected consisted of closed-loop position control. To this purpose, the system was fitted with an encoder placed on the output shaft of the motor-gearbox assembly. The encoder installation had been designed in such a way that the variation in system backlash could be reproduced in a controlled manner in order to be able to observe its effects on the actuator response.

The comparison of the data received from the model with those acquired from the test bench provided a means to verify the soundness of the model. The primary variables tested included position, velocity, and current. In all of these cases, a good degree of accuracy could be observed, both in terms of amplitude and timing. A notable aspect that emerged was the fact that the evolution of deviations between model and bench is concentrated at high values of backlash. However, the high capacity to simulate the behavior of the real system is counterbalanced by the associated computational cost.

Contents

Chapter 1

Introduction

In recent years, a great deal of resources and energy have been spent on the goal to move toward more electric aircraft. With this goal in mind an increasing number of actuation, historically performed by hydraulics, are being performed by electrical systems. The introduction of electric actuation has demonstrated several advantages over hydraulic actuation including:

- Reduced weight.
- Increased efficiency.
- Great flexibility, the routing of the electric distribution system is much easier. This aspect can leads to both increased safety and reduced maintenance costs.
- Reduced number of components.
- Reduced noise.

These benefits can result to a reduction in the overall weight of aircraft, e.g. if all the actuation on the Airbus A300 series could be electrified, it would be possible to save 500kg. Moreover the electric system can be more efficient than the hydraulic counterpart. This improvement can reduce the fuel consumption up to 9% and save 1% of the take-off weight [1].

Another aspect to keep in mind is the costs reduction. Hydraulic system are well known and perform well but the operational and maintenance cost is very high. On the other hand, NASA studies on thrust vector control for solid rocket boosters had shown that the replacement of the hydraulic system with an electric one could save $3M per flight [2]. This kind of improvement is not limited to rocket because studies have shown similar saving on other vehicles.

Unfortunately though, being relatively new in introduction, EMAs lack a knowledge base in comparison to that accumulated for more conventional types of actuators. In this context, a field of particular interest to the aerospace sector and beyond is fault detection and prognosis.

1.1 Electromechanical actuator

Electromechanical actuators generally consist of an assembly of electric motor, power converter and control devices. Power conversion systems are needed because the motor output shaft rotation speed is typically in the thousands, up to tens of thousands, of revolutions per minute with a limited torque. This is due to the fact that the external dimensions of the motor are related to the torque output, while the rotational speed is largely independent from them. Given that the sizes are also related to the weight of the motor it is preferable to use gearboxes in order to meet torque requirements while maintaining a similar power output. With this architecture, the high angular speed at the motor output is reduced to a more usable speed of 50-60 degrees per second for primary flight controls and 5-6 degrees per second for secondary flight controls.

Electromechanical actuators can be classified into two main categories:

- Linear EMA: actuators capable of converting rotary motion

into linear motion, thus providing an actuation similar to a hydraulic piston.

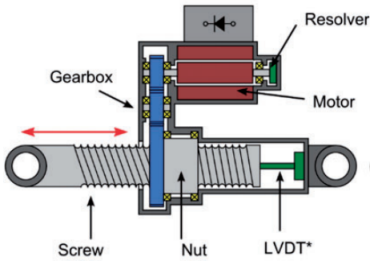

Figure 1.1: *Linear EMA*

- Rotative EMA: actuators providing a rotary output in which the motor is generally combined with a mechanical gearbox.

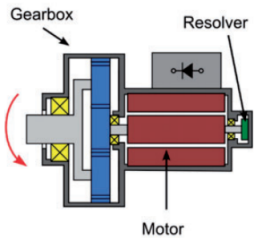

Figure 1.2: *Rotative EMA*

When converting rotary motion into linear motion, the most prevalent solutions involve the use of screw-nut couplings. In the aerospace industry this mechanism is rarely constructed using sliding screw solutions. Friction and wear effects rise dramatically as a result of sliding, which can lead to coupling degradation and, as a result, the development of backlash and instability. For these reasons, recirculating ball systems are widely spread. This system consists of a continuous row of tiny balls running inside a circular helical track, transferring loads with as low as possible friction. However, there are issues with this technique, such as the potential of jamming and slippage of the balls. If the diameter of the spheres is too tiny, rollers solutions are preferable.

The use of rollers instead of balls allow for greater load transfer and very high transmission ratios while reducing the number of parts needed and the complexity of the system.

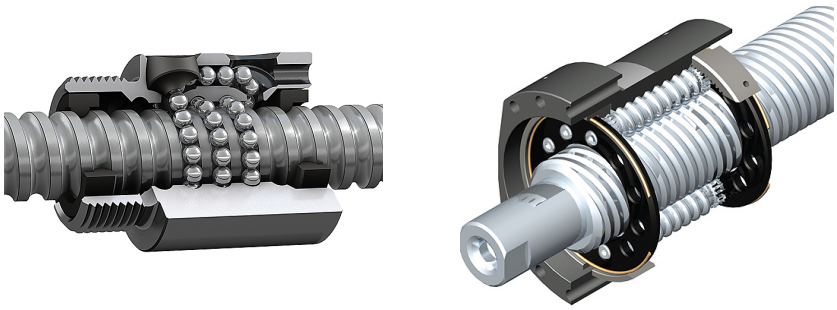

(a) *ball screw* **(b)** *roll screw*

Figure 1.3: *Jackscrew architectures*

Electromechanical actuation fits perfectly in the fly-by-wire architecture minimizing the required power conversions and the overall number of components. The pilot sends a command to the system, which causes Actuator Control Electronics (ACE) to generate an error signal by comparison with the signal received from a Linear Variable Displacement Transducer (LVDT). The presence of the LVDT allows the device to know its current position, enabling it to adapt more easily to the load and control conditions. The error signal, after being amplified and filtered for noise compensation, is used to regulate the system. The signal generated by the ACE is then sent to the Power Drive Electronics (PDE) which also has as input three-phase AC or any other voltage chosen as power supply. The PDE then adjusts the power supplied to the electric motor based on the magnitude of the feedback received from the motor and the command received from the ACE. As mentioned before, the motor can then be coupled with a transmission in order to meet torque requirements and if necessary convert the motion from rotary to linear.

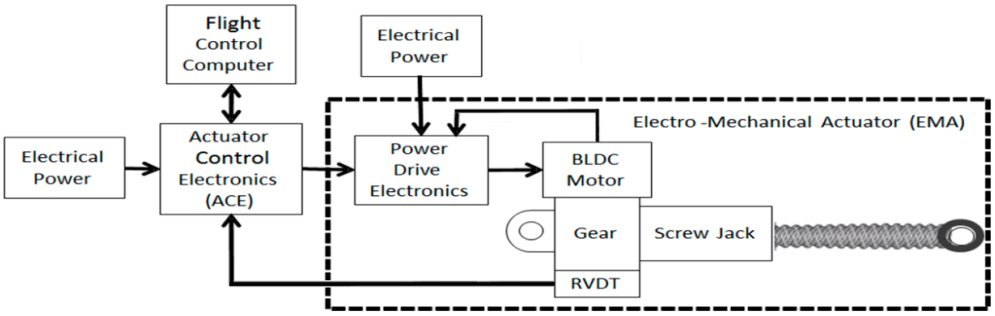

Figure 1.4: *EMA Diagram*

At present, the use of this type of actuator is limited to non-safety critical functions. This is due to the limited knowledge of the type of failures of these actuators and the difficulty of power management (both electrical and thermal). Examples of EMA use can be the actuation of spoilers, horizontal stabilizer trim and high lift devices on the Boeing 787 Dreamliner, or the steering system for the nose wheel on the F-16 Fighting Falcon [1].

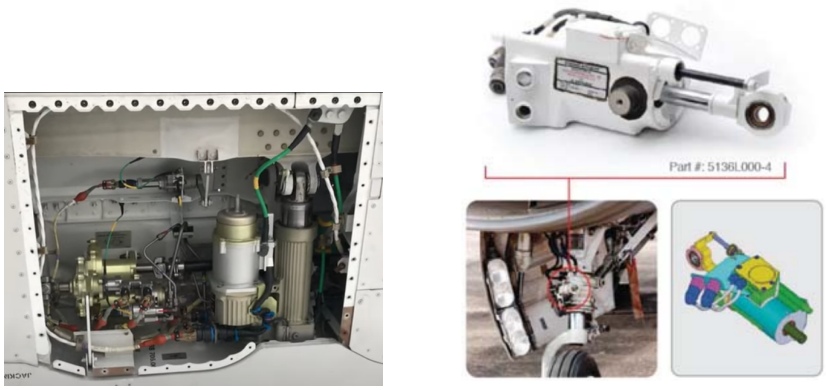

(a) *Boeing 787 Dreamliner* **(b)** *F-16 Fighting Falcon*

Figure 1.5: *EMA currently in use*

With regard to failure modes FMECA(Failure Modes, Effects, and Criticality Analysis) study on EMA actuators has identified the main failure modes and their occurrence rates. The main results are shown in the following table:

Table 1.1: *FMECA for EMA*

Component	Failure rate [h^{-1}]	Failure mode
Bearings	1.78 x 10^{-5}	Increased friction due to: • bearing wear • galling
Position sensor	1.70 x 10^{-5}	Loss/incorrect feedback signal from resolver: • turn-to-turn short • turn-to-ground short • open circuit
Brushless DC motor	1.03 x 10^{-5}	Breakdown of stator assembly insulation due to: • turn-to-turn short • phase-to-phase short • turn-to-ground short • open circuit
Power connector	6.64 x 10^{-7}	Electrical open due to: • open pin • open lead-wire

Source: [3]

1.2 Prognostic

Prognosis may be understood as the generation of long-term predictions describing the evolution in time of a particular signal of interest or condition indicator, with the purpose of estimating the remaining useful life (RUL) of a failing component/subsystem. [3]

In most fields of engineering and in the aerospace industry

in particular, Prognostic Health Management (PHM) had gained attention as a potential meas for monitoring the safety, maintenance and cost of complex systems. PHM has the ability to produce major improvements in aspects such as operational and support cost (O&S) and total life cycle cost of ownership (TOC) without neglecting the ability to optimize system availability. It also allows for safe operation of the various systems as the health of the system is continuously assessed and estimated over a period of time to allow for optimal maintenance. However, one of the most difficult aspects of prognosis is the "large-grain" uncertainty that is inherent in the prediction of future behavior. Long-term fault prediction, up to the point when a failure might occur, necessitates the ability to describe and manage the inherent uncertainty.

The approach to the problem of prognostics can be divided into two main categories: data-driven and model-based. Both approaches had their own set of benefits and drawbacks thus they're frequently employed in conjunction in order to benefit from the best features of each of them.

1.2.1 Data-driven techniques

The data-driven techniques are generated directly from operational data of systems that are constantly monitored. In many systems, actual input/output metrics are the primary opportunity to know more about the system evolution and response. The data-driven techniques are based on the hypothesis that statistical properties are predominantly influenced by system faults. This assumption leads to the data-driven approach being dominated by statistical analysis and pattern recognition techniques.

The distinctive aspect of the data-driven strategies is to turn high-dimensional noisy data into lower-dimensional information. This step increases the amount of knowledge that can be derived from the single piece of data, making the evaluation of

system conditions easier. On the other hand, being derived from data, means that the effectiveness of the data-driven approach is strongly reliant on the quantity and quality of operational data.

1.2.2 Model-based techniques

Model-based approaches are based on the possibility to define a sufficiently accurate mathematical model. This kind of approach is based on the evaluation of the difference between the measurements performed on the real system and the results provided by a mathematical model. The hypothesis is that in the presence of faults this differences, also known as residuals, are big. On the other hand, under nominal conditions, with only noise and modeling mistakes, the residuals are limited.

A characteristic feature of this kind of approach is that it is able to incorporate knowledge of the basic operating principles of the system to be monitored. At the same time, this technique allows the model to be adapted to take into account different types of system degradation as its understanding increases.

In conclusion, this method allows the system's behavior to be captured with greater precision than data-driven methods, a fidelity that is met by the need to solve a model whose complexity is highly dependent on the type of system to be monitored.

Chapter 2

Model description

In order to develop an algorithm capable of identifying faults conditions of an electromechanical actuators it is necessary to develop a numerical model capable of accurately reproduce the behavior of real components. Particular attention has been paid to the possibility of reproducing the behavior of a system characterized by a reaction time between those of a primary flight control and those of a secondary flight control.

With this objective in mind, the model developed in Matlab-Simulink adopts an integration step of 1×10^{-6} s. This choice makes it possible to faithfully model the behavior of the electronic part of the system while remaining one or two orders of magnitude below the characteristic time of the electronic side (which shows the shortest characteristic time).

Given the need to reproduce the behavior of the system over long time intervals, a fixed step integration method has been adopted. In particular ODE 1, also known as Euler's method, has been adopted; this choice, although more demanding in terms of computational resources, has a lower cost in terms of memory required.

2.1 Data flow

The whole system models a position-controlled actuator, consequently the “Com” block output represent a position signal to the “Control electronics” subsystem. This component models the behaviour of the actuator control electronics: outputs a current whose intensity is governed by the error between the commanded and actual position of the actuator and the actual motor speed. The signal produced by such a component is then sent to the “Inverter model” subsystem. The inverter subsystem, combining the position provided by the “Resolver” subsystem and working in conjunction with the “Electromagnetic model” subsystem, produces the supply voltages for the different phases of the motor. The “Electromagnetic model” subsystem makes it possible to assess the currents circulating in the various phases of the motor, taking into account the impact of motor-transmission dynamics. Such effects are derived from the “Motor-transmission dynamical model” subsystem, a module in which external resistance forces and driving forces determine the position and angular velocity of the motor-gearbox assembly. The last component, the “Signal acquisition” subsystem, provides the direct current and quadrature current from the currents circulating in the each of the three phases.

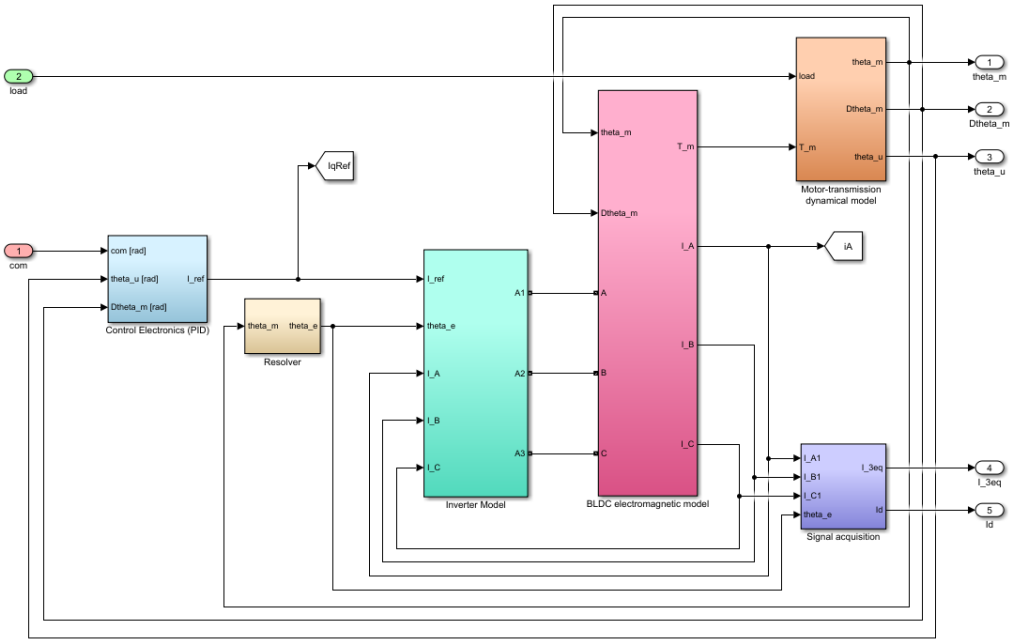

Figure 2.1: *Top level model overview*

2.2 Electro-mechanical actuator model

2.2.1 Command block

The block “Com” allows to define the type of position command to test the model.

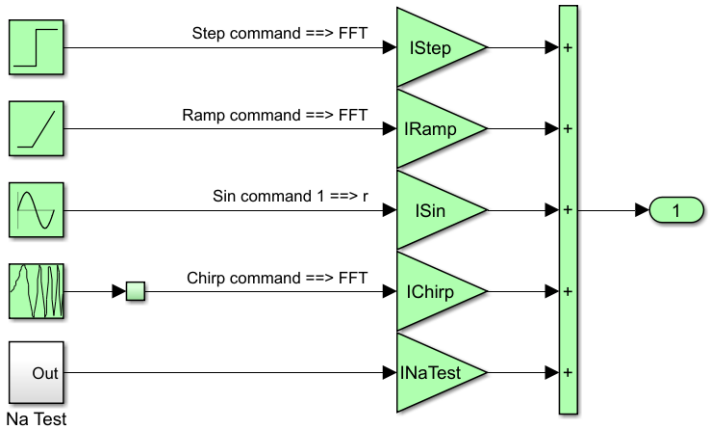

Figure 2.2: *Command block*

It allows to produce commands such as step, ramp, sine wave

or chirp and also to combine them with each other. This large selection of command allows to reproduce a wide range of conditions of operation of the real component subject to simulation.

2.2.2 Load block

The "Load" block applies a resistive load to the model in reference to a time history.

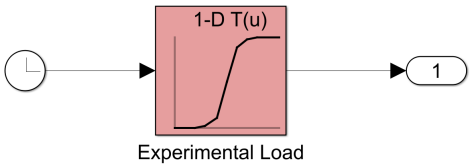

Figure 2.3: *Load block*

This subsystem allows therefore to expose the entire model to the effective resistant force obtained from the experimental tests, thus reproducing in a more faithful way the behavior of the real system.

2.2.3 Control Electronics subsystem

This subsystem models the behavior of the actuator's control electronics.

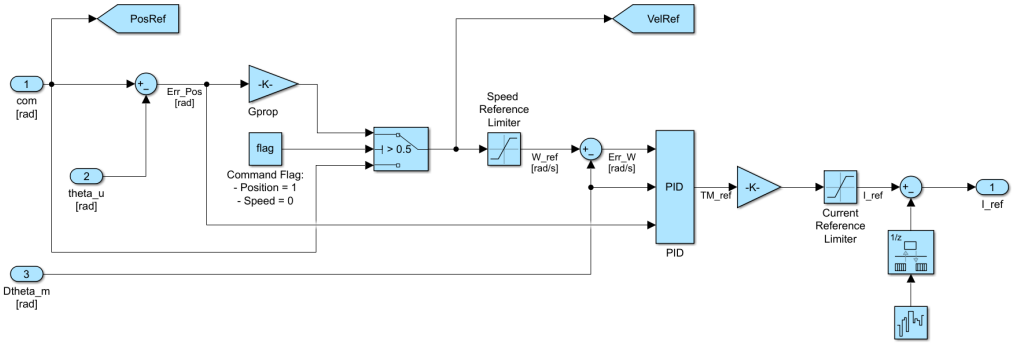

Figure 2.4: *Control Electronics subsystem*

In particular, it receives as input the commanded position and by comparing it with the actual one generates a position error.

After this error signal is amplified by a proportional gain, a reference speed can be calculated. By comparing the reference speed with the actual speed of the motor, it is now possible to generate the speed error signal. The signals representing the speed error, the motor speed and the position error are then sent to the "PID" block which outputs the reference current value.

Important limitations on the values of the variables involved are introduced in this subsystem. The first limitation is placed on the actuation speed while the second on the current required to satisfy the command. These two limitations represent the limitations on the ability of the magnetic circuits of the motor to reach adequate values in the required time and of the power electronics to tolerate high currents.

PID

Within the "PID" block, there are three distinct branches: proportional (P), integrative (I) and derivative (D).

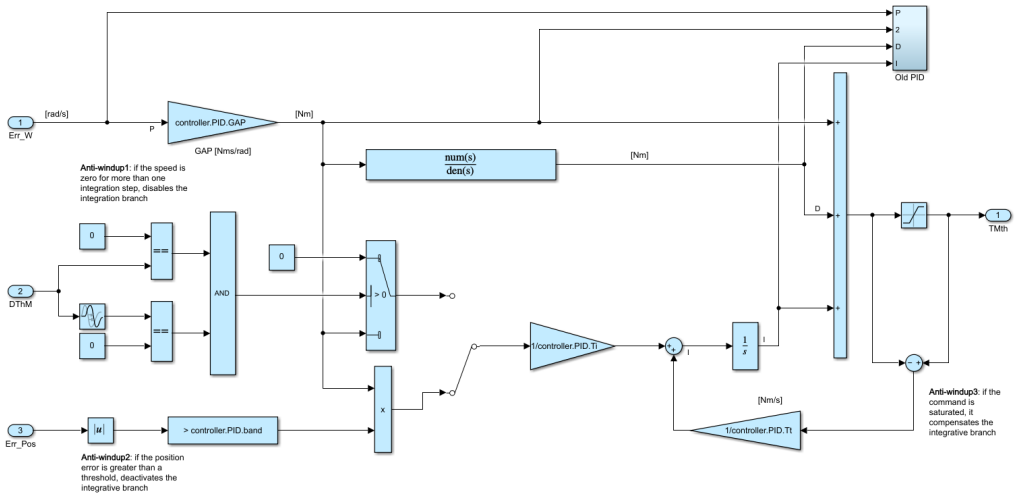

Figure 2.5: *PID block*

The proportional branch simply amplifies the signal from the velocity error by a constant term. The derivative branch resorts

to the use of the following transfer fiction:

$$f(s) = \frac{T_d s}{\frac{T_d}{N} s + 1}$$

where:

- T_d = characteristic time of the derivative branch
- N = derivative filter bandwidth

This technique in fact makes it possible to reduce the number of components used and at the same time reduces the effect of noise amplification on the signals that a numerical derivation would introduce. By application of block diagram algebra, it is possible to demonstrate how the adopted transfer function is fully equivalent to the following architecture:

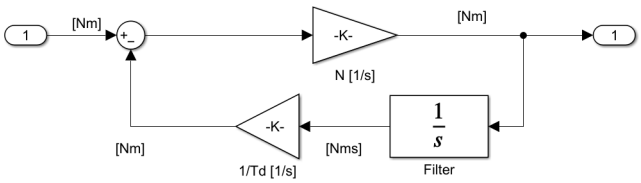

Figure 2.6: *PID architecture*

The integrative branch generates a signal related to the integral of the position error. This branch is revealed to be the most critical as the interaction of the signal with the saturations of the system can lead to the windup phenomenon. Integral windup occurs as a saturation for the system makes impossible to reach the desired value of the signal. This nonzero error is integrated by this branch thus resulting in a condition where the output signal from the PID controller is dominated by the integrative component. The model described introduces three different anti-windup solutions:

- **Anti-windup 1**
  In this solution, the system analyzes the motor speed. In case the velocity is zero for more than one integration step, the system excludes the integrative branch.

- **Anti-windup 2**
  In this solution, the system analyzes the position error. In case the position error is greater than an a predefined band, the system excludes the integrative branch.

- **Anti-windup 3**
  In this solution, the system analyzes the error between the ideal and saturated output signal. In the case of a saturated condition, the difference between the two signals produces an error that appropriately multiplied by the gain of the integrative branch is used to reduce the integrative contribution.

The solution adopted during the simulations appears to be the third as the first two have some limitations. The first solution is limited by the fact that it is possible for the system to come to a stop condition for more than one integration step at a position far from the desired value. This condition may lead to the deactivation of the integrative branch precisely in a condition where its contribution is more influential than the proportional and derivative ones. The second solution is limited by the definition of the value of the band within to nullify the integrative contribution. This choice must be made prior to the simulation and therefore poorly adaptable to different conditions.

In conclusion, the saturated sum of the torques of the proportional, integrative and derivative branches is the motor reference torque provided as output by the PID block.

2.2.4 Resolver block

The "Resolver" block allows to obtain the electrical angular position knowing the mechanical angular position.

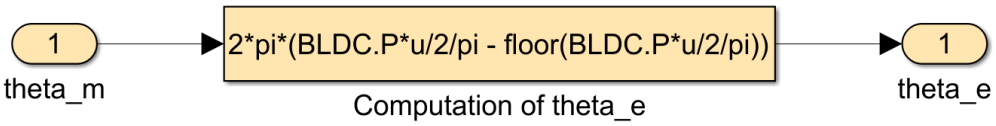

Figure 2.7: *Resolver*

The electrical angular position is in fact linked to the mechanical one through the number of motor poles pair. The generic expression is therefore:

$$\theta_e = N_p \theta_m$$

where:

- θ_e = electrical angular position
- N_p = mechanical angular position
- θ_m = motor poles pair

In this particular model the formula used is slightly more complex as it introduces a limitation on the possible output values of the position between 0 and 2π.

2.2.5 Inverter model

The "Inverter model" subsystem takes the reference current from the "Control electronics" and the electrical angular location of the motor from the "Resolver" block in order to determine the actual current circulating in the different phases of the motor.

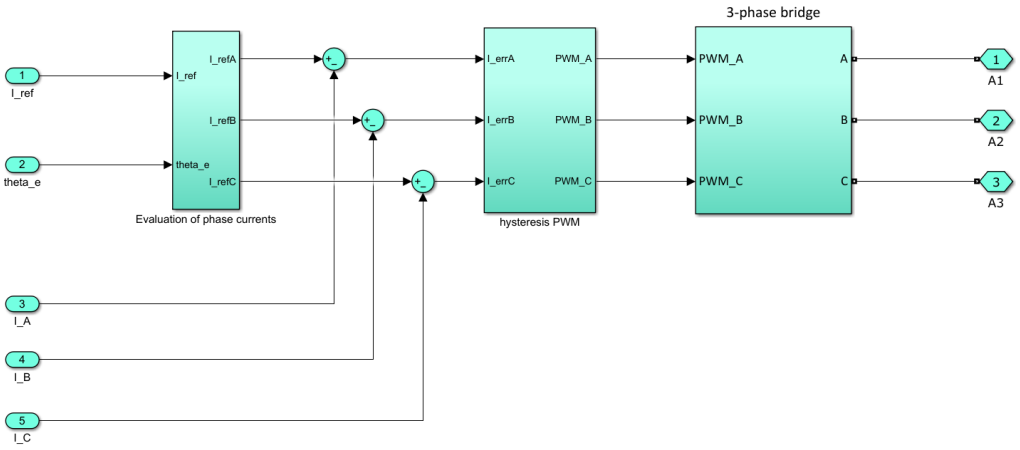

Figure 2.8: *Inverter model*

The motor's reference current and angular position are fed into the "Evaluation of phase currents" subsystem, where the single phase reference current originated from the "Control Electronics" subsystem is converted into the reference current for each phase using the inverse Clarke-Park transformation, with a null direct reference current. The reference current on each individual phase is then compared with the electric current actually circulating the phase thus producing an error.

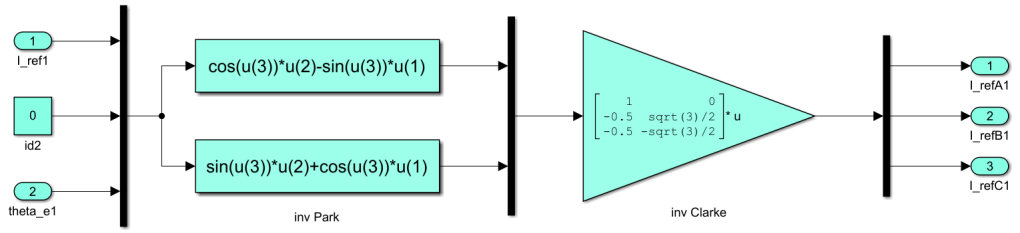

Figure 2.9: *Clarke-Park inverse transformation*

The error signal is then sent to the "Hysteresis PWM" block in which it is used to make the duty cycle determination of the PWM signal powering the motor. The use of hysteresis blocks makes it necessary to accurately define the dead-band. Particular attention should be paid to avoid aliasing, the Nyquist-Shannon theorem states that the PWM carrier frequency must be at least

10 times higher than the phase switching frequency. When compared to standard Pulse Width Modulation implementations, this PWM modeling is a simplification. In truth, the error on each current is often supplied to a PID controller, which regulates the actual switching between phases, but in this case, it was chosen to design a simpler but effective solution for computational reasons.

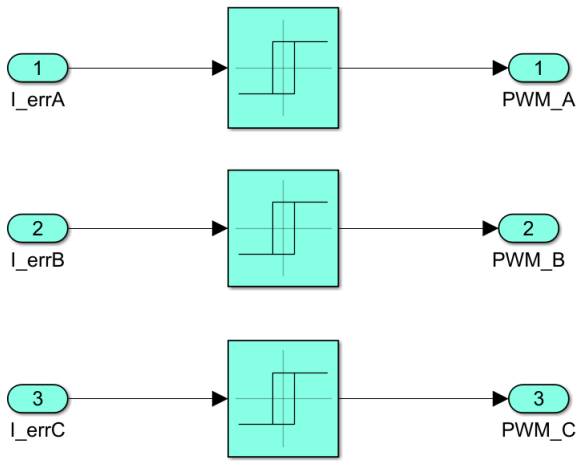

Figure 2.10: *Hysteresis PWM block*

The last component of this subsystem models the behavior of the power electronics that power the different phases of the motor, the "3-phase bridge" reproduce a static H-bridge (MOFSET) power converter. For each of the three phases, the subsystem receives a Boolean signal as input. Each signal's original value and its inverse are determined. These are the elements of the vector that the "Universal Bridge" block require as a control input. The switching of the power transistors is coordinated based on the value assumed from the elements of such vector and three voltage signals are generated as output to the subsystem. The "Universal Bridge" block is also connected to a DC voltage source that symbolizes the inverter subsystem's power supply.

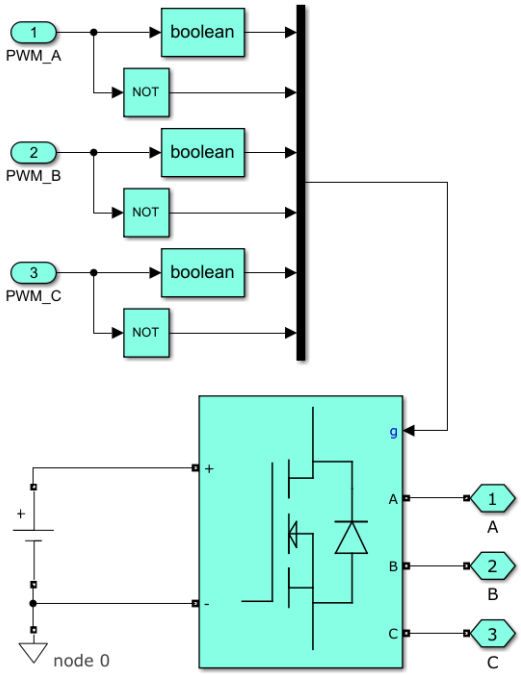

Figure 2.11: *H-bridge power converter model*

2.2.6 BLDC Electromagnetic model

This subsystem simulates the electromagnetic behavior of the motor and allows the determination of the torque produced.

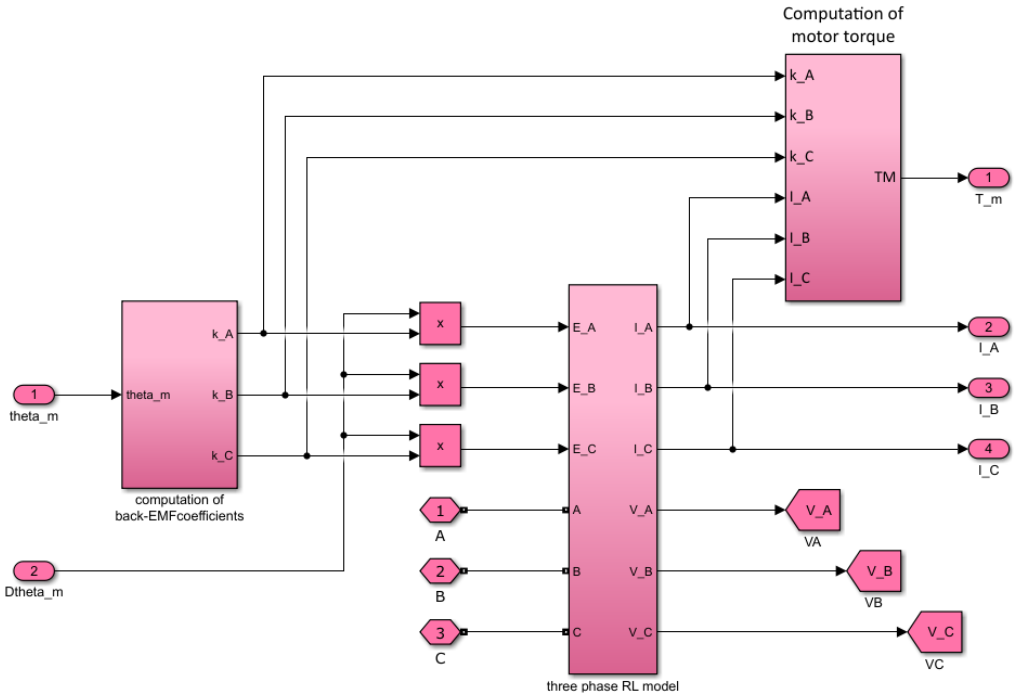

Figure 2.12: *BLDC Electromagnetic model*

Similar to what happens in the "Resolver" subsystem, the mechanical angular position of the motor is received as input and transformed to the appropriate electrical angular position. The nominal counter-electromotive force constants for each motor phase are then derived from the electrical angle of the motor using the "Effect of rotor PM field density" blocks. The following section labeled "Effect of static eccentricity (zita,phi)" represents a correction that allows for the inclusion of faults such as partial stator coil short circuit or influence of rotor static eccentricity.

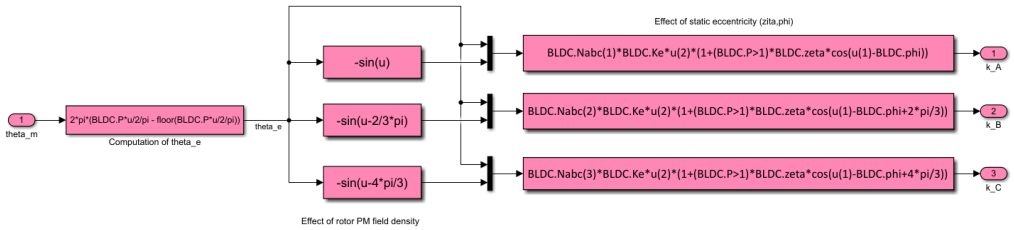

Figure 2.13: *Computation of Back-EMF coefficients block*

The three counter-electromotive force constants are then multiplied by the motor's angular speed signal in order to generate the value of the counter-electromotive force acting on each of the individual phases. The now know counter-electromotive force is then passed to the "three phase RL" subsystem, which by resorting to modeling using Simscape blocks reproduces the electrical behavior of the motor wingdings. The circuit represents a star architecture in with the dominant contributions of each phase being inductive and resistive.

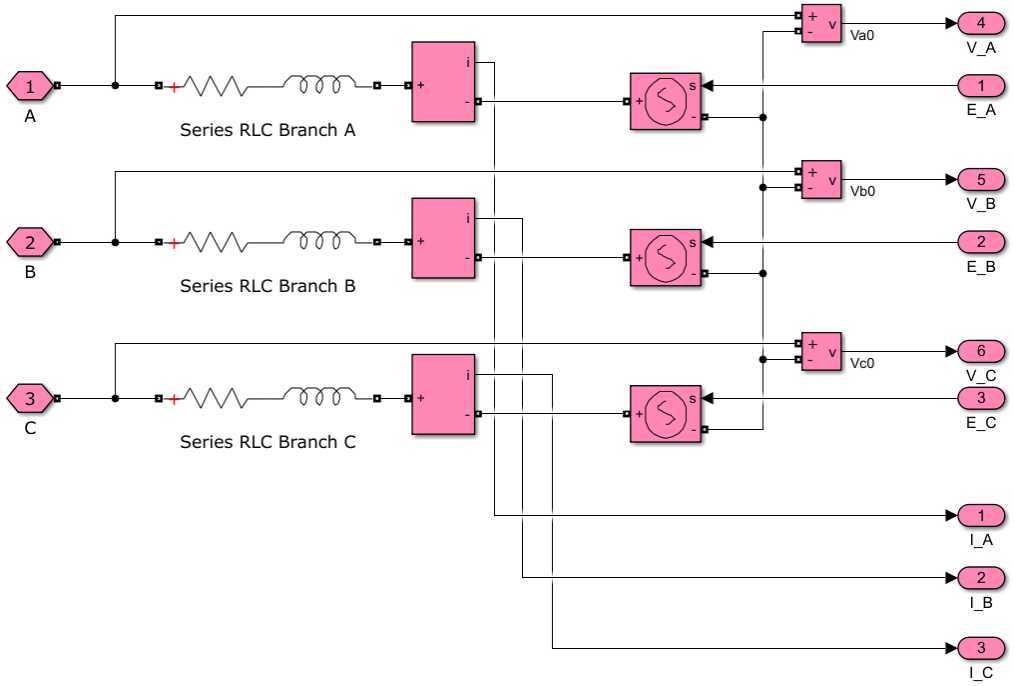

Figure 2.14: *Three phase RL model*

It is important to note that given the ability to reproduce the behavior of winding subject to partial short-circuit, the inductive and resistive terms of the phases involved must be corrected to account for the number of turns in nominal operation, resulting in:

$$R_i = RN_i$$

$$L_i = LN_i^2$$

Where:

- R, L = nominal value
- R_i, L_i = effective value
- N_i = fraction of active coils

The effect of counter-electromotive force is modeled with the insertion of a voltage generator on each of the phases. The different phases are therefore subject to a voltage that is reduced by a term that is governed by the counter-electromotive force constants obtained from the block “Back-EMFcoefficients”.

The last important parameter to be determined within the “BLDC Electromagnetic model” subsystem is the torque produced by the motor. The torque is in fact determined in the block in place for the “computation of motor torque”. The product of the counter-electromotive force constant and the actual current present on each phase is computed to determine the value of the torque produced for each phase and subsequently summed to establish the total value generated by the machine. This final value is then saturated to reflect the torque limitations that the engine exhibits.

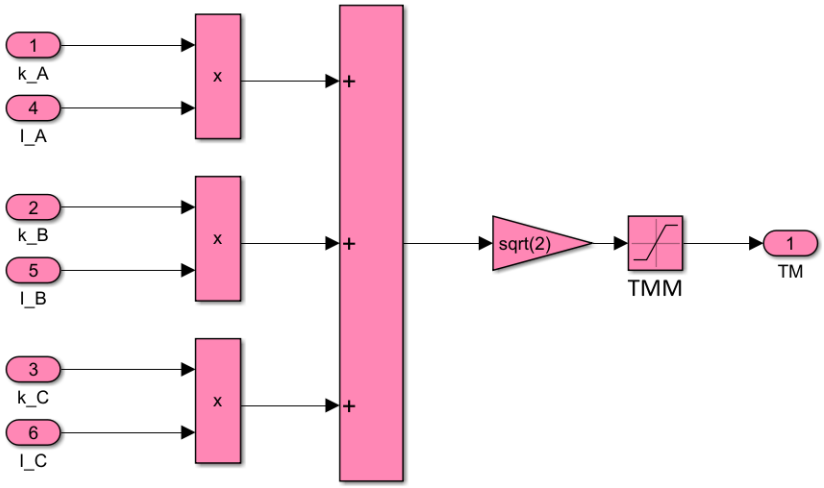

Figure 2.15: *Computation of motor torque block*

2.2.7 Motor-transmission dynamic model

In this subsystem, the interaction of the torque generated by the motor with the resisting torques is modeled in order to evaluate the kinematic variables of the motor-transmission system.

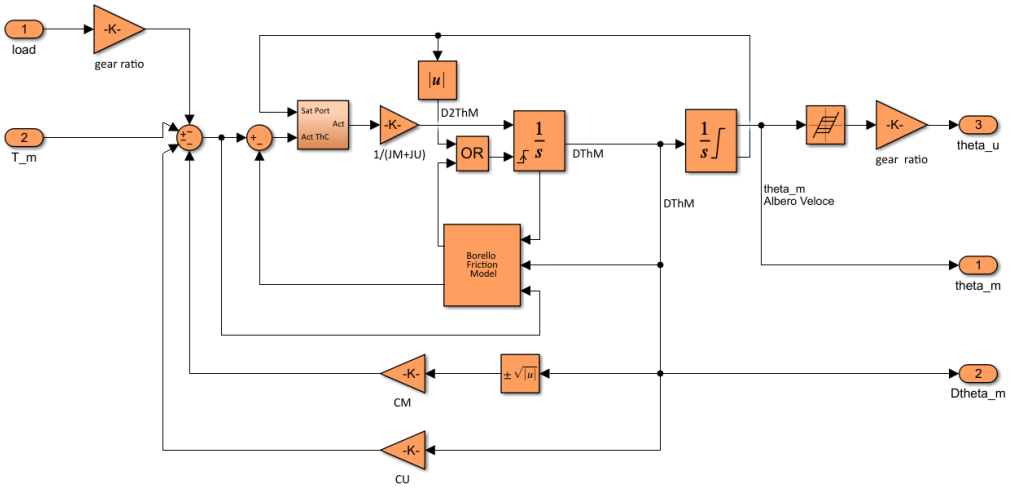

Figure 2.16: *Motor-transmission dynamic model subsystem*

The first step is to refer torques in the same shaft, in this case the fast one. For accurate modeling of dynamic behavior, it is also important to estimate the viscous resistance component. This evaluation is performed by multiplying the motor's angu-

lar speed by a viscous damping coefficient representing the viscous behavior of the whole motor-user system. The residual torque acting on the system along with the rotation speed at different integration steps is then provided to the block "Borello friction model" in order to simulate the effects of friction. The use of the Borello friction model is due to the fact that it allows with greater accuracy and simplicity to reproduce critical system behaviors. In particular, it allows for accurate discrimination between static and dynamic friction conditions, thus enabling the best reproduction of the system's stopping and restarting conditions.

The "Borello friction model" block is divided into two main branches, one responsible for evaluating dynamic friction and the other for evaluating static friction. The discriminating variable between the activation of one or the other branch proves to be the velocity at the current integration step. In the case where the velocity is found to cross the null value, the branch responsible for static friction is activated and at the same time the velocity of the integration block is set to zero. This allows for a verification of static friction conditions. In the event that the static friction forces exceed those produced by the motor, the system will maintain the position reached, while in the opposite case the system will resume motion subjected again to dynamic friction.

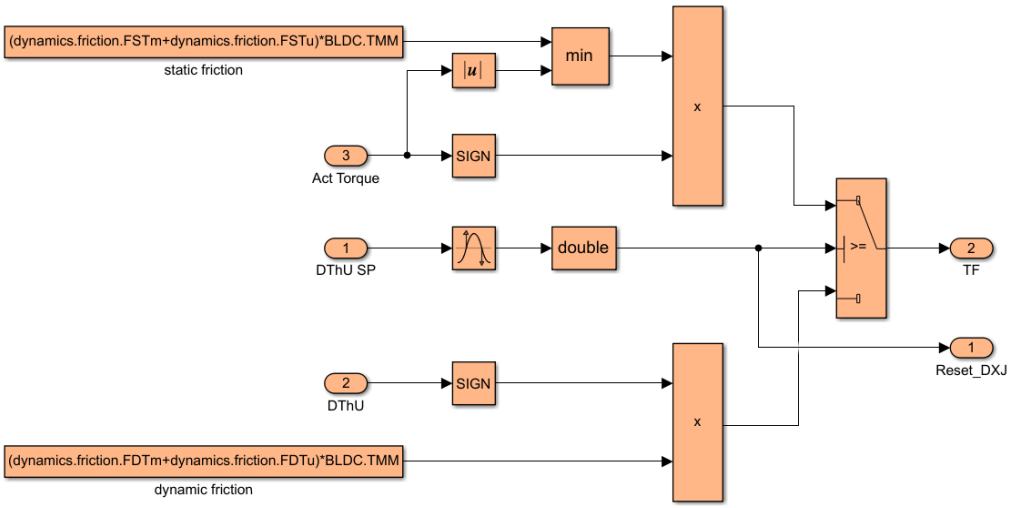

Figure 2.17: *Borello friction model*

This subsystem also reproduces the behavior of mechanical limit stops. This effect is reproduced through a signal flag from the integrator responsible for position determination. This integrator, being saturated, allows the output position value to be limited, also making available a signal flag to make its status known (upper limit exceeded, not limited, lower limit exceeded). This signal flag is then used to override the velocity and to determine the acting constraint reactions.

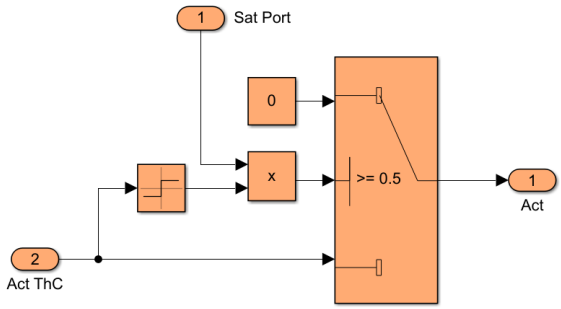

Figure 2.18: *Constraint reaction model of mechanical limits*

The last effect reproduced in this subsystem results in backlash. This effect is reproduced by inserting a special block whose effect is to restrict the output in case the input value changes tendency.

2.2.8 Signal acquisition subsystem

The "Signal acquisition" block allows the direct and quadrature current to be obtained knowing the currents on the individual phases and the electrical position of the motor.

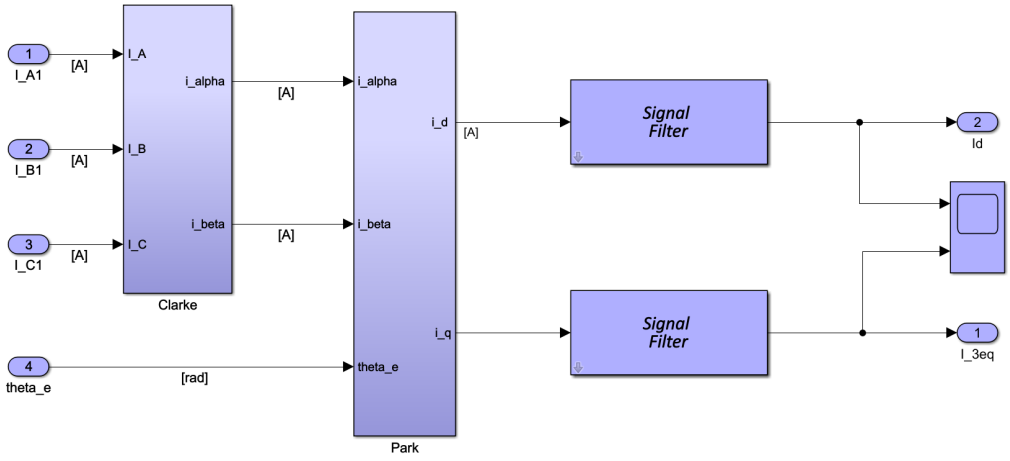

Figure 2.19: *Signal acquisition subsystem*

Its operation is similar to that of the subsystem that allows the evaluation of currents in the phases within the "Inverter model". In this case, however, instead of using the inverse Clark-Park transformation, the direct one is used.

Chapter 3

Test bench description

In order to verify and validate the correct operation of the model presented in the previous chapter, it is necessary to arrange an experimental test bench to which compare the results produced by the simulation.

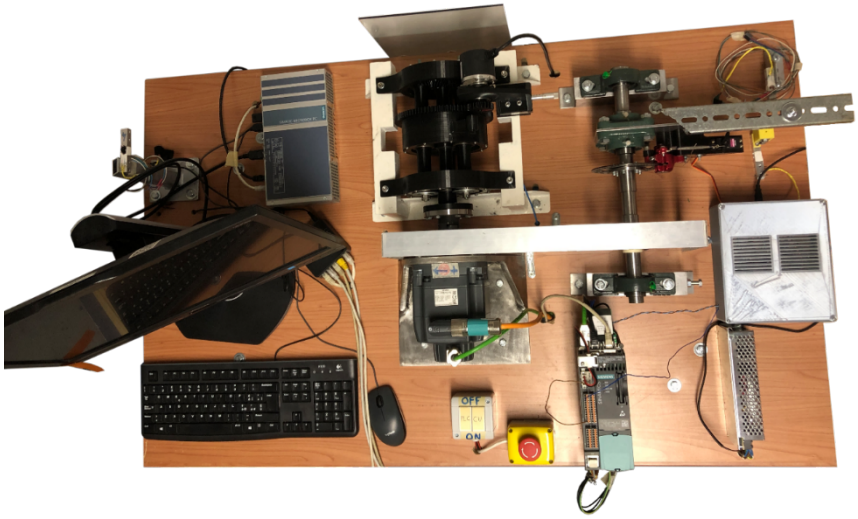

Figure 3.1: *Test bench picture*

The resulting test bench design can be divided into two main parts, the part in charge of the actuation and the part in charge of generating the resistive load. The part in charge of executing the command results in the motor-gearbox assembly and

the necessary control and power electronics. The part, on the other hand, dedicated to generating the resistive load turns out to be composed of a shaft on which a brake is mounted and the actuation with his electronic controller in charge of monitoring the applied resistive load. The two assemblies are then connected by a chain sprocket transmission. All components that go into the part that represents the actuator (excluding the transmission) are components of industrial origin. These components share the same architectures and failure modes with their aerospace counterparts but at the same time are easier to find and adapt to custom uses.

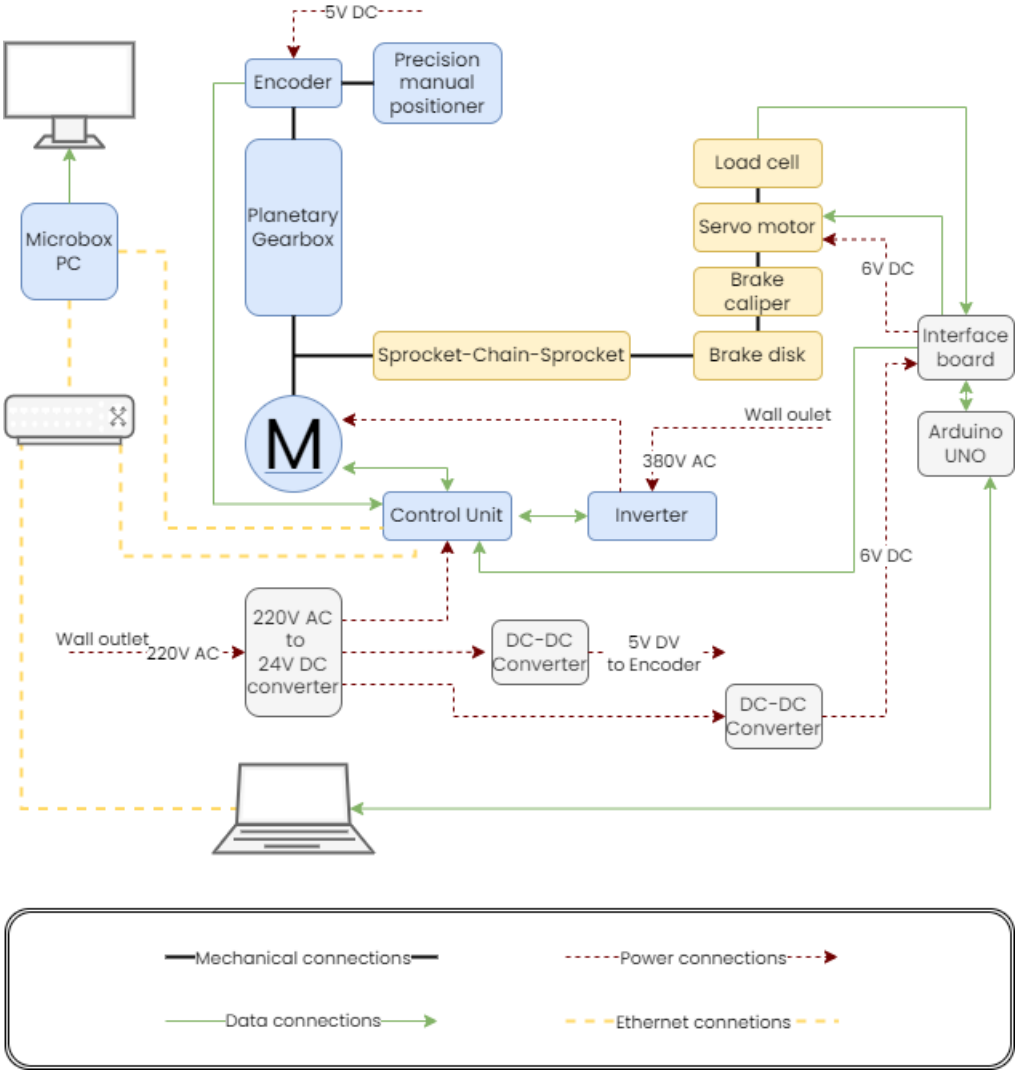

Figure 3.2: *Test bench diagram*

3.1 Actuator assembly

The actuator module consists mainly of elements developed by Siemens, such as the Microbox PC, Control Unit, and Power Module, which enable the Sinamics S120 PMSM motor to be controlled at will. The only component developed in-house is the planetary gearbox connected to the output shaft of the motor. The operation of this group of elements is governed by the Microbox PC where is virtualized the PLC responsible for the high-level logic for position command tracking. The reference positions are then sent to the Control Unit whose main task is to drive the attached inverter to power the motor. The transmission is then connected to the output shaft of the motor, which as a result of appropriate angular speed reduction puts the end-user encoder into rotation.

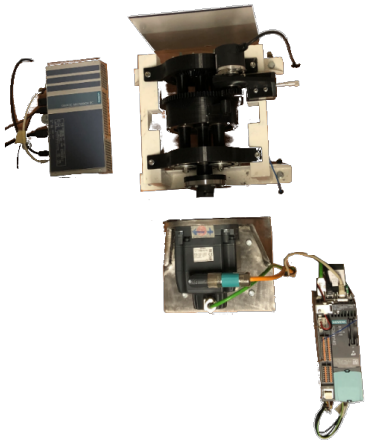

Figure 3.3: *Actuator assembly*

3.1.1 SIMATIC Microbox PC

The main processing and control unit of the actuation system constituted by the Siemens elements consists of the SIMATIC IPC427E Microbox PC.

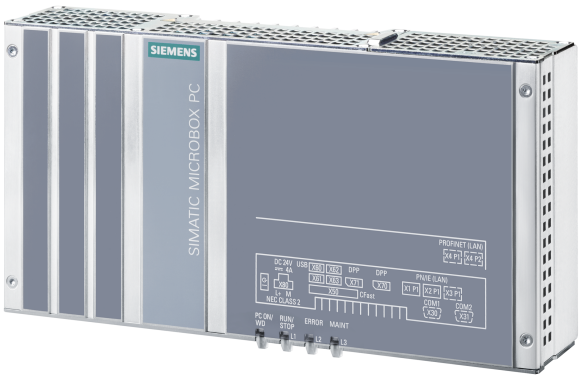

Figure 3.4: *SIMATIC IPC427E Microbox PC*

This component consists of a passively cooled compact PC developed to provide processing capabilities in direct proximity to controlled machinery. For this reason, it is designed to be an excellent platform for applications ranging from application virtualization to data acquisition and analysis.

Table 3.1: *Microbox PC technical specifications*

Installation type	DIN rail, wall mounting
Power supply	24V DC (max 4A)
Processor	Intel Core i3-6102E
Memory	16 Gbyte DDR4-SDRAM SO-DIMM
Storage	128 Gbyte SATA SSD
Interfaces	3x industrial Ethernet (RJ45)
	4x USB port (USB 3.0)
	2x serial COM (RS 232/485/422)

Continued on next page

Table 3.1: *Microbox PC technical specifications (Continued)*

	2x Display Port
IP degree of protection	IP20
Ambient temperature during operation	0°C to 55°C
Dimensions	Width 262 mm
	Height 139.7 mm
	Depth 55.5 mm

In the particular architecture adopted, its task is to virtualize the PLC and run the server required for command management. The control server, accessible through a web portal, allows for broader control possibilities. In fact, thanks to specialized compilers, it is possible to create control logic in Matlab language far more complicated than what is possible at the PLC level.

3.1.2 SINAMICS Control Unit

The controll unit consist of the CU310-2 PN (PROFINET).

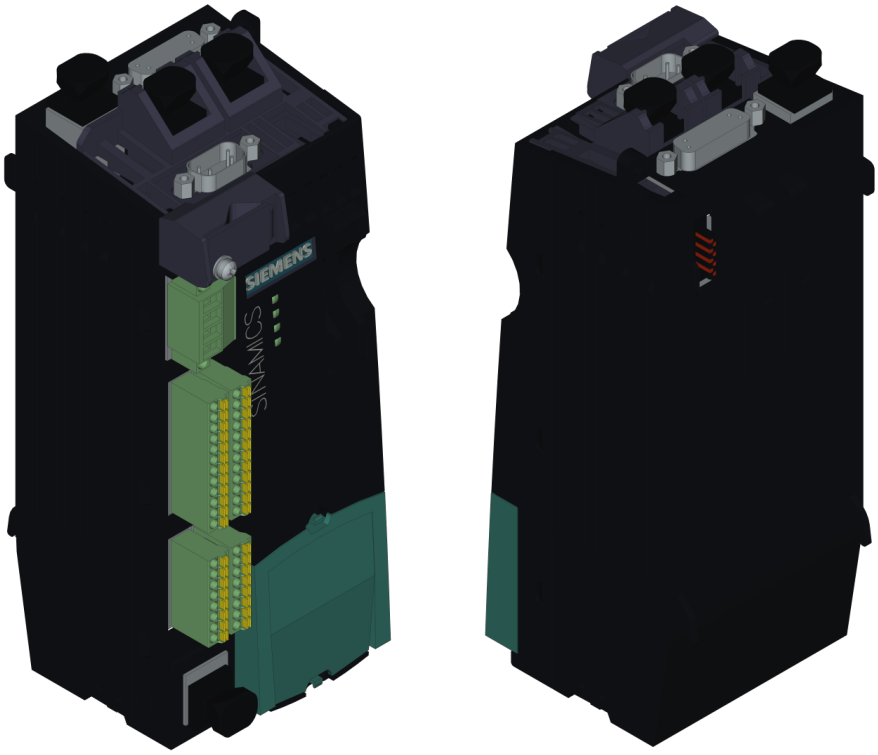

(a) *front* **(b)** *back*

Figure 3.5: *SINAMICS CU310-2 PN control unit*

This component consists of a processing and control device connected directly to the power supply unit. This element interfaces via direct connection with the power unit on which it is mounted and features a wide range of peripherals to interface with various sensors.

In the adopted architecture it results to be connected via Ethernet cable to the PLC and the encoder embedded in the motor while receiving data from the encoder located on the gearbox via serial interface. The CU while connected to the PLC is able to operate autonomously thanks to the ability to mount a memory card that allows the installation and storage of custom firmware.

For example, it is possible to perform motor speed control in both open loop and closed loop. As is already the case with the Microbox PC, the CU is powered at 24V DC in order to standardize the power supplies to the various control components and minimize the need for dedicated power supplies.

Table 3.2: *SINAMICS Control Unit technical specifications*

Power supply	24V DC (max 0.8A)
Interfaces	3x PROFINET[1]
	1x DRIVE-CLiQ[2]
	1x Ethernet/IP
Encoder interface	incremental encoder TTL/HTL or encoder SSL without incremental signals
Encoder frequency, max	300 kHz
Number of digital Inputs	11
Number of digital I/O	8
Digital signals voltage	-3V to 30V
Digital signals low level	-3V to 5V
Digital signals high level	15V to 30V
Number of analog input	1
Ambient temperature during operation	0°C to 55°C
Dimensions	Width 73 mm
	Height 191 mm
	Depth 75 mm

[1] *Real-time implementation of ethernet comunication*

[2] *Siemens proprietary communication interface*

3.1.3 SINAMICS Power Module

The power management component is a SINAMICS PM240-2 Power Module.

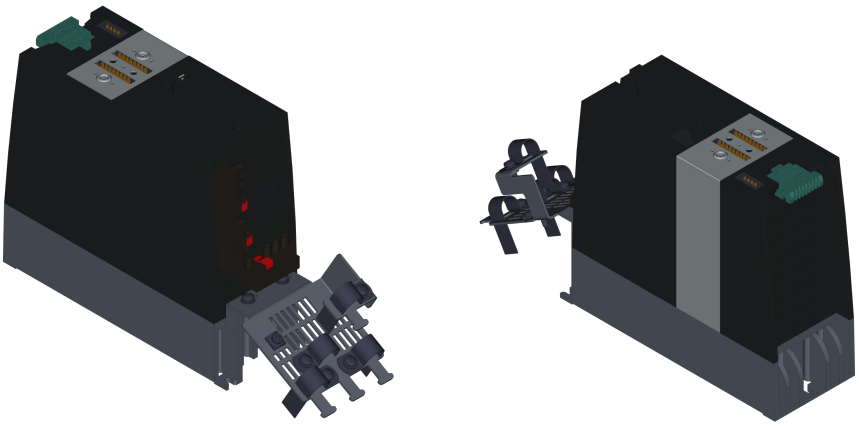

(a) *front* **(b)** *back*

Figure 3.6: *SINAMICS PM240-2 Power Module*

This component consists of an air-cooled modular inverter powered with 380V AC and directly driven by the CU. The peculiarity of this element is to integrate a diode rectifier, an inverter, and the ability to dissipate braking currents on external resistor banks in a single component.

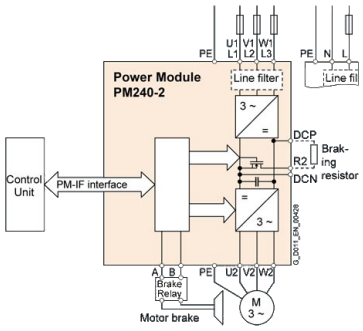

Figure 3.7: *Electrical diagram*

Table 3.3: *SINAMICS Power Module technical specifications*

Input	
Number of phases	3 AC
Line voltage	380V to 480V
Line frequency	47 Hz to 63 Hz
Rated current	2.00 A
Output	
Number of phases	3 AC
Pulse frequency	4 kHz
General specifications	
Power factor	0.85
Efficiency	0.96
IP degree of protection	IP20
Cooling	Internal air cooling
Ambient temperature during operation	-5°C to 40°C
Net weight	1.50 kg
Dimensions	Width 73 mm
	Height 196 mm
	Depth 165 mm

3.1.4 SIMOTICS Synchronous Motor

The engine installed on the test bench is a SIMOTICS S 1FK7060-2AC71-1CG0 synchronous motor.

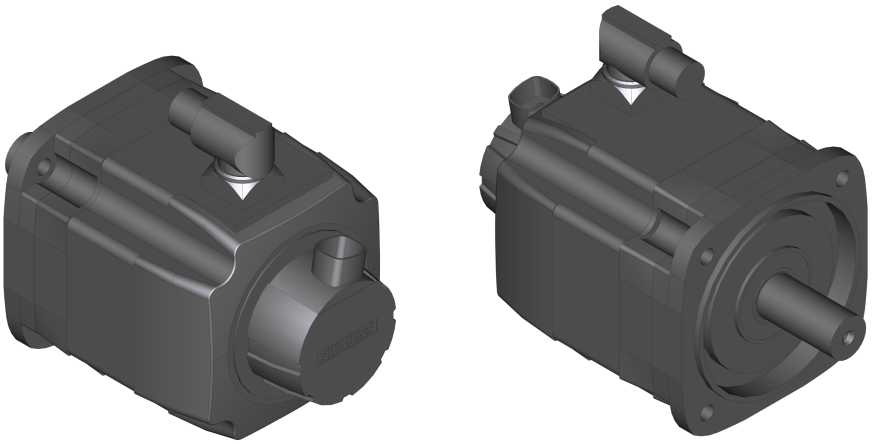

(a) *front* **(b)** *back*

Figure 3.8: *SIMOTICS Synchronous Motor*

The 1FK7 motors are lightweight permanent magnet motors with heat dissipation through the motor surface in such a way as to avoid the need to provide external cooling. The motor incorporates an absolute encoder built into the structure and used by CU in order to appropriately drive the currents on each of the individual phases.

Due to the thermal design choice, operating temperatures are limited in order to preserve the proper functioning of the electrical and magnetic components. In order to keep the motor within these operating temperatures, the torque that can be delivered is limited and in any case tied to the speed of rotation.

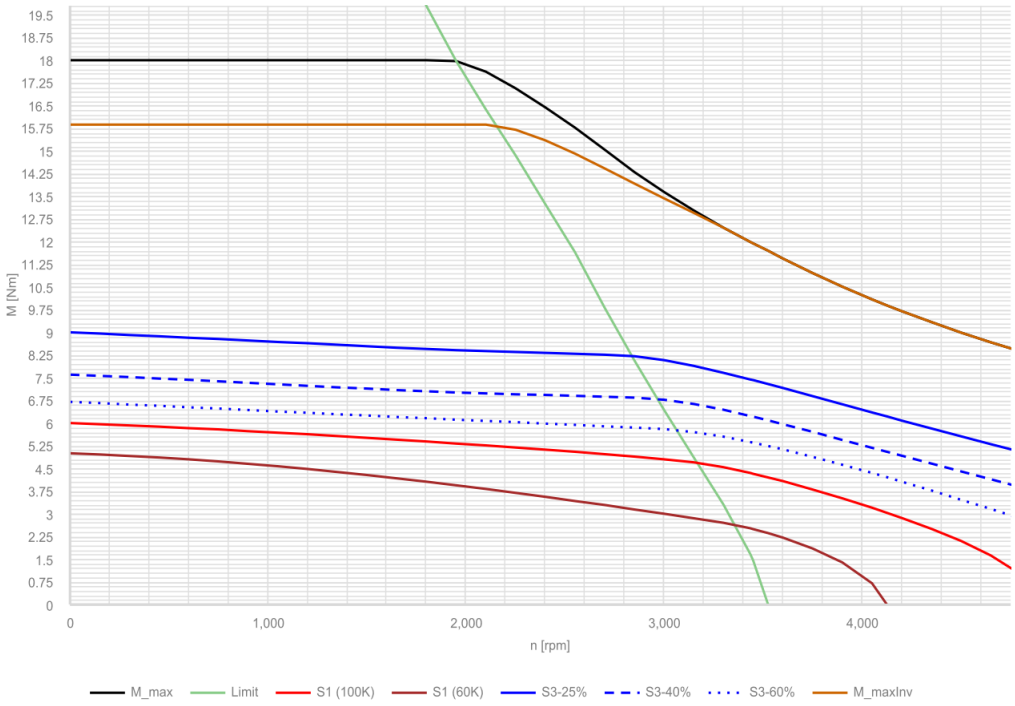

Figure 3.9: *SIMOTICS S-1FK7 motor characteristics*

In terms of continuous operations, the characteristic S1 (100K) defines the upper limit of the permitted operation with a component working temperature of 155°C. A second condition of continuous operation is represented by the curve S1 (60K) defined in such a way as to maintain the component at a temperature of 90°C. Thus, the S1 (60K) curve provides a safer alternative and makes it possible to avoid conditions where increased temperature could adversely affect the operation of the component. Intermittent operation is described by the curves S3-25%, S3-40% and S3-60%. In this areas, depending on the activation of each phase, a higher load can be delivered by the motor while maintaining a 155°C over-temperature limit. Under any operating condition the maximum torque that can be delivered by the engine is nevertheless lower than M_max.

In addition to limitations due to operating temperatures, there are also limitations on rotational speeds. The limits on rotational speeds are mainly due to electrical and mechanical causes. The

electrical causes are due to the ability of the power electronics to switch with high frequencies required by high rotational speeds while the mechanical causes are due to the ability to withstand the centrifugal forces produced in the moving parts.

Table 3.4: *SIMOTICS motor technical specifications*

Motor type	compact permanent-magnet synchronous motor
Number of poles	8
Rated current	3.0 A
Efficiency	0.90
Degree of protection	IP64
Cooling	natural cooling
Temperature monitoring	Pt1000 temperature sensor
Encoder system	Encoder AM24DQI: absolute encoder 24 bits (resolution 16777216) + 12 bits multi-turn
Net weight	7.1 kg
Motor characteristics	
Rated speed (100K)	2000 rpm
Rated torque (100K)	5.3 N m
Static torque (100K)	6.0 N m
Stall current (100 K)	3.15 A
Static torque (60K)	5.0 N m
Stall current (60K)	2.55 A
Electrical and mechanical constants	
Moment of inertia	7.700 kg cm^3

Continued on next page

Table 3.4: *SIMOTICS motor technical specifications (Continued)*

Torque constant	1.91 Nm/A
Winding resistance at 20°C	2.75 Ω
Time constants	Thermal 30 min
	Electrical 11.10 ms
	Mechanical 1.75 ms
Optimum operating point	
Optimum speed	2000 rpm
Optimum power	1.1 kW
Limiting data	
Max. permissible speed (mech.)	7200 rpm
Max. permissible speed (inverter)	4750 rpm
Maximum torque	18 N m
Maximum current	10.7 A

3.1.5 Planetary gearbox

Given that compact motors produce very high angular speeds at the output, a gearbox is almost always needed to increase the torque produced and reduce the angular speed on the user shaft. Because of this the planetary transmission installed on the bench is an high transmission ratios gearbox developed entirely by the Politecnico di Torino. Its peculiarity is that it was produced using additive manufacturing techniques, in particular it was produced using FDM (Fused Deposition Modeling) techniques in order to ensure fast development time and low production costs.

Figure 3.10: *Pictures of the planetary gearbox*

The structure of the transmission consists of a central input shaft surrounded by three planetary gears enclosed in a support ring. Those planetary gears are located on the same shaft on which are mounted secondary stage gears that are responsible for setting the output ring in motion.

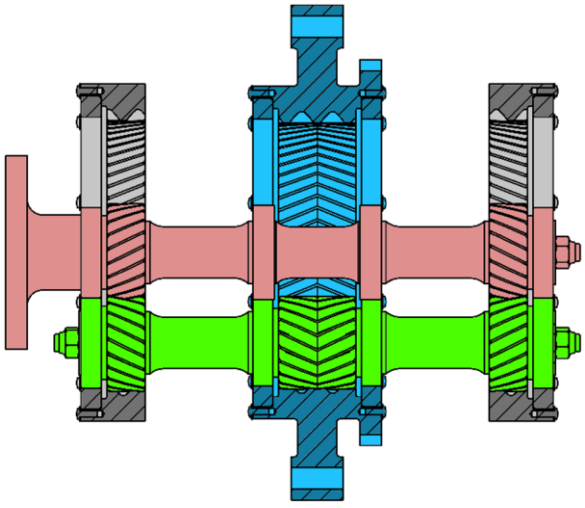

Figure 3.11: *Section of the gearbox: input shaft (red), planetary gear (green), output ring (blue), mounting ring(gray)*

One of the most important features of this planetary gearbox design is that the first stage is mirrored to ensure a balance between the forces discharged on the satellites. As a result of this solution, a planet carrier is not required because no torque or force is applied to it. A second distinguishing feature is the use of helical teeth, which can handle axial loads in both directions. This design choice combined with a symmetrical orientation of the teeth results in self-supporting planetary shaft that do not require bearings.

Gearbox property determination

The gearbox design geometry can be summarized as follows:

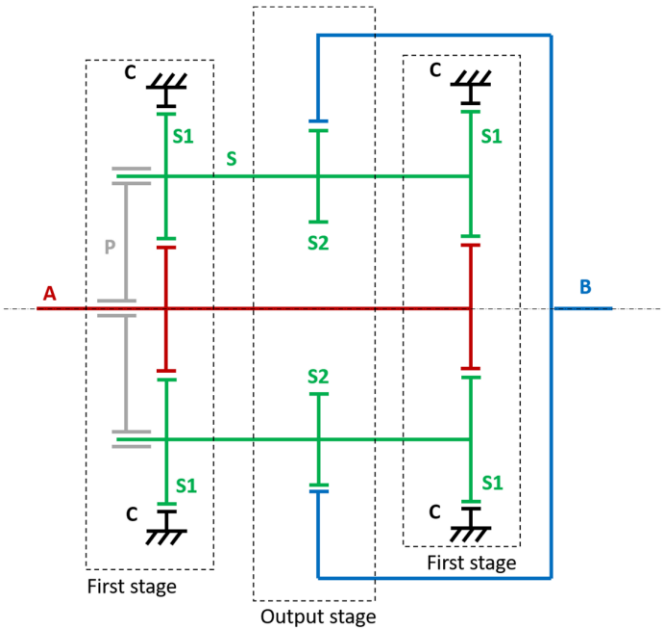

Figure 3.12: *Gearbox geometry layout*

Table 3.5: *Number of teeth for gear*

Z_A	21
Z_{S1}	21
Z_{S2}	20

Continued on next page

Table 3.5: *Number of teeth for gear (Continued)*

Z_C	63
Z_B	62

Given these parameters, the Willis's equation can be used to determine the overall gear ratio. Willis's formula in fact constitutes a general relationship that makes it possible to determine the gear ratio of the rotism from the number of teeth of the wheels that are composing it.

$$\tau_w = \frac{\omega_2 - \Omega}{\omega_1 - \Omega}$$

where:

- τ_w = gear ratio
- ω_1 = sun gear angular speed
- ω_2 = ring gear angular speed
- Ω = planet carrier angular speed

Assuming that the various wheels possess the same modulus, since there can be no sliding of one between the others, it is possible to replace the angular speeds with the number of teeth. For the two stages of the transmission gearbox is obtained as follows:

$$\tau_1 = \frac{\omega_A - \Omega}{\omega_C - \Omega} = \frac{Z_C}{Z_A}$$

$$\tau_2 = \frac{\omega_A - \Omega}{\omega_B - \Omega} = \frac{Z_B Z_{S1}}{Z_A Z_{S2}}$$

Where for the first stage it is imposed that the angular speed of the ring gear is zero. As a result, the final gear ratio turns out to be:

$$\tau = \frac{\omega_A}{\omega_B} = \frac{1 + \frac{Z_A}{Z_C}}{\frac{Z_A}{Z_C} - \frac{Z_A Z_{S2}}{Z_{S1} Z_B}}$$

In order to estimate the transmission moment of inertia, the density and length of the structure were assumed to be of unitary value. Instead, for the geometric characteristics, sprockets were equated with their primitive circumferences while the outer radius of the gear wheel B was assumed to be 20% larger than the inner radius. Therefore, it is possible to write the moments of inertia of the different components as:

$$I_A = \frac{1}{2} M_A r_A^2$$

$$I_S = \frac{1}{2} M_S r_P^2$$

$$I_B = \frac{1}{2} M_B (r_B^2 + (1.2 r_B^2)^2)$$

where:

- M_A = input shaft and sun gear mass
- M_B = output ring gear mass
- M_S = planet gear mass
- r_A = sun gear radius
- r_B = ring gaer radius
- r_P = planet carrier virtual radius

Finally, by reducing all the different moments of inertia at the input shaft, it is possible to obtain the overall moment of inertia of the transmission, which comes out to be 1.75 x 10^3 g mm^2.

Table 3.6: *Gearbox technical specifications*

Manufacturing technique	FDM
Material	PLA
Reduction ratio	124
Inertia reduced to input shaft	1.75 x 10^{-6} kg m^2

Continued on next page

Table 3.6: *Gearbox technical specifications (Continued)*

Max torque	2.3 N m
Ultimate torque	10.8 N m $\pm$ 10%

3.1.6 Encoder

The encoder installed on the gearbox output shaft is a high-resolution optical incremental encoder, specifically the TSW581HS model.

Figure 3.13: *TSW581HS encoder*

It makes it possible to perform closed-loop position control of the motor with a degree of resolution that allows the effects of backlash to be observed. The optical type of encoder is very popular due to its simplicity of construction and reliability. These devices are in indeed comprising three main components: a light source, a spinning disk, and a photo-detector. Given the incremental nature of the adopted encoder, it allows only to determine changes in position with respect to an initial condition. In order to determine position changes only two output signals are needed, labeled channels A and B. The two encoder output channels show both the position and the direction of rotation by using two coded disk with sectors that are out of phase. Discrimination of the direction of rotation is done by observing which of the two channels has a leading signal while the position is mea-

sured by counting the signal fronts of both channels.

The characteristics of the encoder located on the user output are summarized in the table below.

Table 3.7: *Encoder technical specifications*

Part number	TSW581HS.M2.5000.5.V.K4.B127.PL10.PP2-5
Resolution	5000
Output frequency	up to 300 kHz
Continuous speed	6000 rpm
Degree of protection	IP64
Ambient temperature during operation	-10 °C to 70 °C
Net weight	0.25 kg
Moment of inertia	40 g^2 cm
Electrical characteristics	
Power supply	5V DC (max 150mA)
Output circuit	Push-Pull 5V output only
Protection	short circuit (no limit duration)
Mounting	
Shaft	⌀12.7 mm
Type	spring M2
Optimum operating point	
Flange	Aluminum
Housing	Polyamide
Shatf	Stainless steel

In order to make it possible to fine-tune the measured backlash, it was decided to install the encoder on a movable stand.

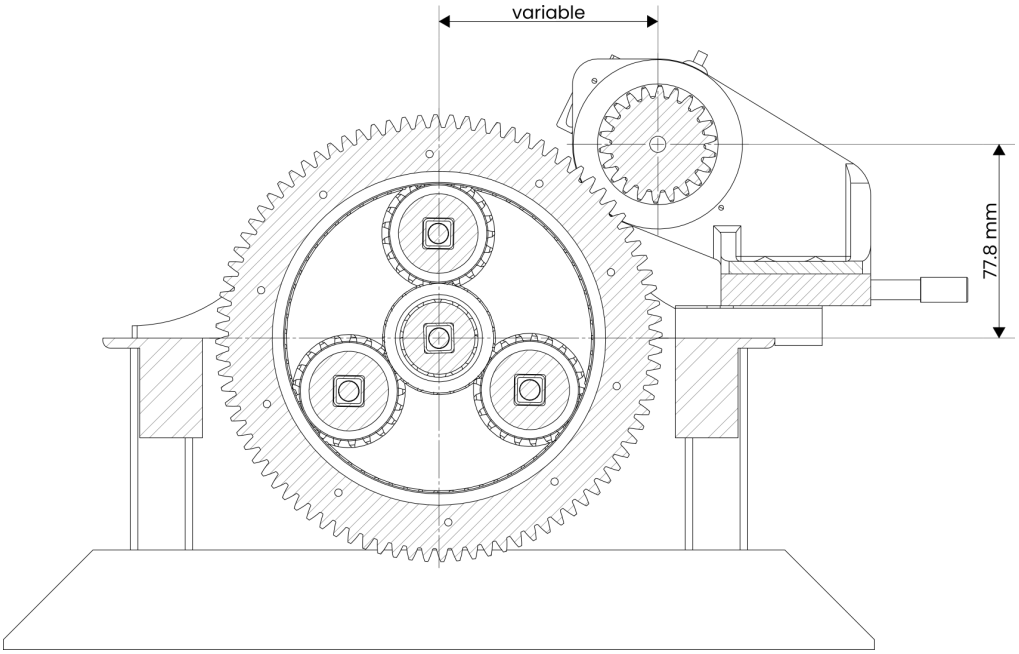

Figure 3.14: *Movable stand*

The support structure thus turns out to consist of three main parts: the attachment element to the gearbox support structure, the micro-mover and the angled encoder support. The attachment element to the structure provides a necessary adapter between the different attachment systems of gearbox and micro-mover and also allows for accurate and repeatable positioning of the assembly. The micro-mover then allows accurate measurement of the distance traveled by the encoder support structure. The support structure of the encoder has an inward angle in order to place the encoder gear at 45° in relation to the output gear of the reduction. The choice of orienting the structure in this way allows the sensitivity of the micro-mover to be increased, thus making it possible to measure even minimal backlash.

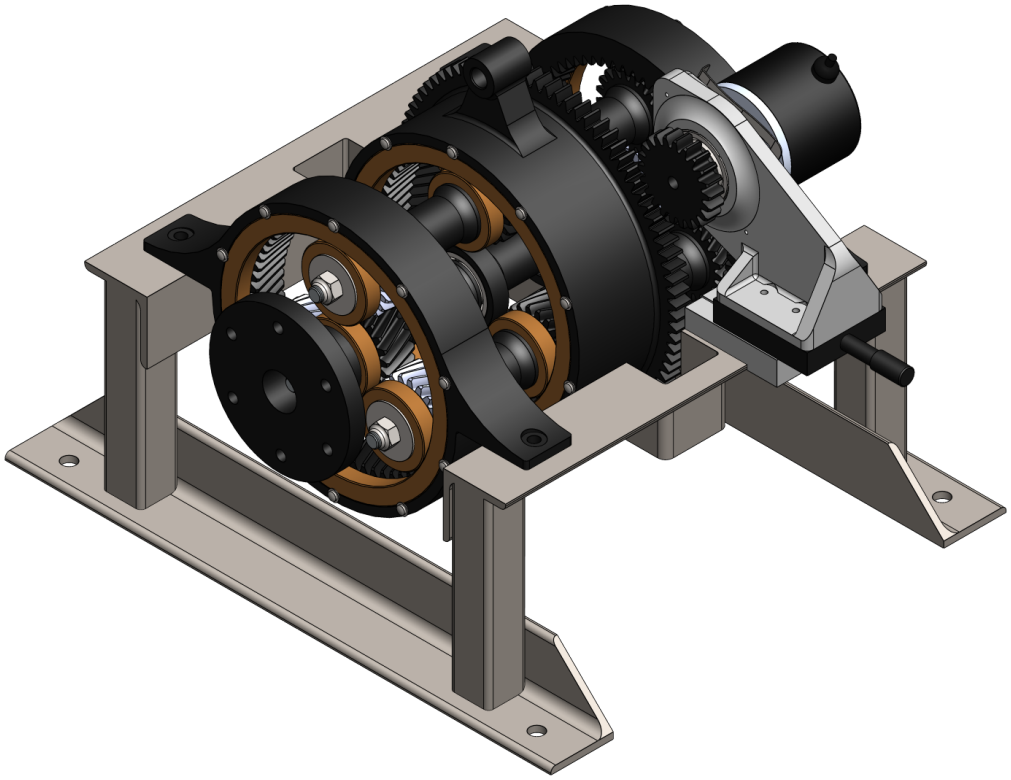

Figure 3.15: *Encoder-Gearbox assembly*

3.2 Resistive load assembly

This module consists mainly of a shaft on which a braking device is mounted and a chain transmission for connection with the actuator module. The operation of this group of elements is governed by an Arduino microcontroller responsible for monitoring the torque applied.

3.2.1 Bracking shaft

The braking shaft is the component responsible for generating the resisting torque. The main element installed on this shaft is a disc brake, the stationary part of which is mounted on a stand for accurate measurement of the torque exerted.

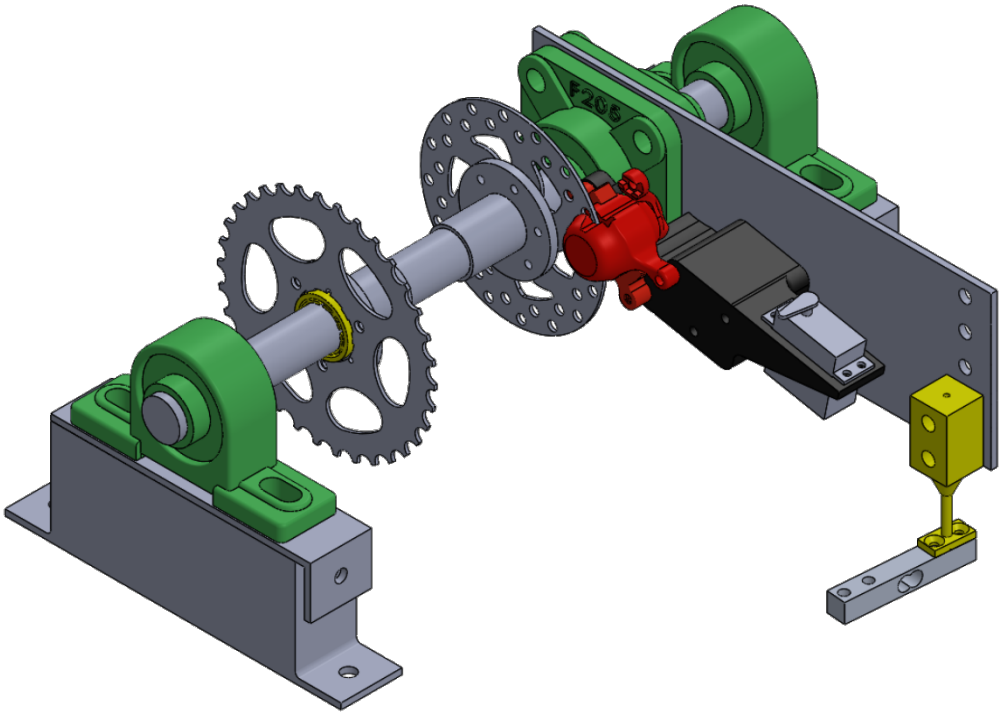

Figure 3.16: *Braking shaft assembly*

In detail, the assembly consists of a shaft placed parallel to the actuator shaft supported by two self-aligning bearings. Attached to the shaft are both a gear wheel and the brake disc. The sprocket constitutes part of the chain transmission that connects the actuator shaft with the brake shaft, while the brake disc is the rotating element of the brake module. In close proximity to the brake disc there is a metal plate held in place by two self-centering bearings placed on the brake shaft. Such plate forms the mounting element for all the static elements of the brake. In particular, on it is mounted the support for the brake caliper and the servo-actuator that actuates the brake caliper. Brake caliper and necessary servo-actuator are finally connected by an adjustable rigid rod that allows necessary corrections to be made to compensate for brake pad wear.

The use of a rotating plate for the attachment of all static brake elements allows measurement of the torque acting on that component simply by measuring the forces applied by the plate on

the connection to the test bench surface. Connection to the bench is then made by means of a plastic rod connected to a load cell by means of a hinge designed to minimize internal friction but at the same time allow transfer of both compressive and tensile loads.

The brake caliper and servo-actuator assembly is responsible for the application of braking force. For this reason, it was decided to adopt a servo-actuator capable of generating sufficient force on the brake pads and at the same time being able to respond promptly to changes in the required force. The choice therefore fell on a servo motor usually adopted in aeromodeling applications.

Table 3.8: *Brake caliper servo-actuator technical specifications*

Part number	DM5163M
Power supply	4.8V to 6.0V DC (more than 2A)
Torque	15.5 kg cm @ 4.8V
	16.3 kg cm @ 6.0V
Speed	0.15 s/60° @ 4.8V
	0.13 s/60° @ 6.0V
Net weight	58 g
Dimensions	Width 40 mm
	Height 37 mm
	Depth 20 mm

In order to ensure precise application of braking force, the servo actuator is controlled by an Arduino UNO microcontroller. This controller by acquiring the force data measured by the load cell connected to the rotating plate allows closed-loop control of the braking force produced. The microcontroller communicating via a serial interface with the user-controlled computer

acquires the value of the desired braking torque. At the same time, thanks to the load cell it is possible, knowing a few geometric dimensions, to reconstruct the value of the torque actually produced by the brake. Known the setpoint and the actual value, it is then possible to calculate the error that is used as the input value for a PI control logic. The signal resulting from the PI control logic consists of the sum of an integrative and a proportional contribution. The integrative branch also features a saturation on the error signal that constitutes a simple but effective anti-windup logic.The control signal is finally saturated as a way to represent the mechanical limitations introduced by the servo-actuator and thus avoid undesirable behavior when the limit positions are reached.

Brake control logic

The resistive torque is controlled through a PI controller with a feedback loop on the force measured by the load cell. The difference between the force required and the force actually measured thus represents the input variable of the PI controller. The signal produced by the controller is then sent to a lookup table that allows a force signal to be converted into a position values by which the servomechanism for brake actuation can be controlled.

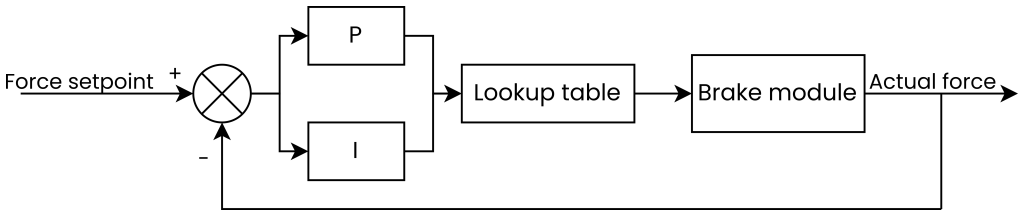

Figure 3.17: *Brake control architecture*

The fundamental element for the operation of the architecture just described is the lookup table. For its definition, a series of different tests were performed. In these tests the position of the brake caliper servomechanism was varied while keeping

the motor at a constant actuation speed of 100 rpm. Under these conditions, the force applied on the load cell was then measured as the commanded position varied, yielding the following results:

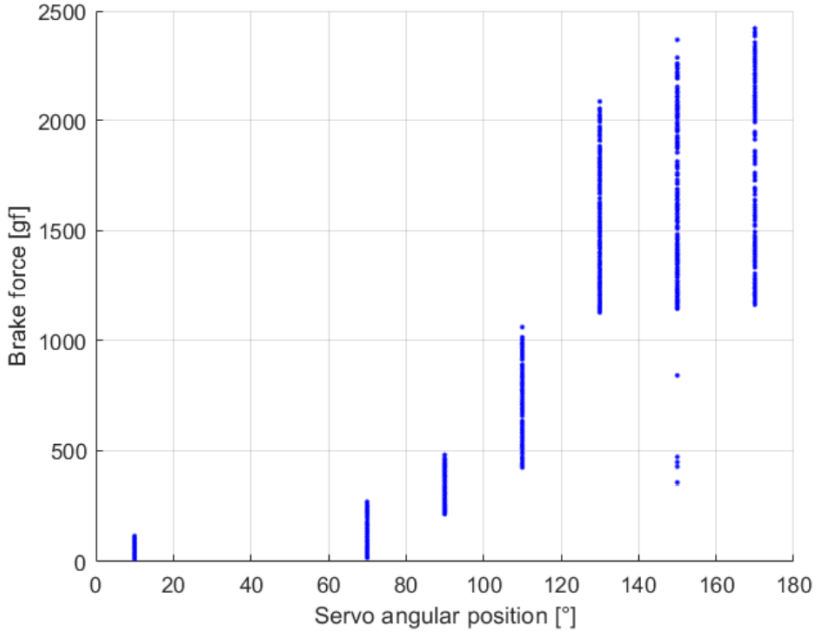

Figure 3.18: *Braking force at different position*

For each position, the mean force value was then calculated and a fit with a hyperbolic tangent was performed, thus obtaining:

$$f(x) = \left[\tanh\left(\frac{x - 115}{35}\right) + 1\right] * 900$$

The inverse function of f(x) can be written thus connecting the force acting on the load cell with the angular position of the servo. This leads to writing the following function:

$$g(y) = \frac{35}{2} \ln\left(\frac{y}{1800 - y}\right) + 115$$

where:

- y = load cell measured force
- g(y) = servomechanism angular position

3.2.2 Chain drive

The chain drive is the component responsible for the mechanical connection between the actuator module and the braking module.

Figure 3.19: *Chain drive*

The use of this type of transmission allows the two shafts to be placed in parallel, rather than in series, and at the same time allows a moderate increase in the resistive torque produced by the braking module. In order to reproduce the dissipative effects present within the actuator gearbox, the connection between the two shafts was placed at the output shaft of the motor. This placement also has the advantage of greatly reduce the stresses to which the transmission is subjected, thus lowering the risk of damaging the delicate components that constitute the transmission made up primarily of plastic material. The choice of a roller chain drive is mainly due to its widespread use, which makes it an element whose behavior is now well understood. In addition, the presence of the rollers around the chain bushings allows high transmission efficiencies to be achieved by minimizing internal friction within the chain. Reducing system friction is indeed a priority in order to precisely control the resistive forces being applied to the motor.

The gear ratio of this linkage is easily determined once the teeth numbers of the two gear wheels is known.

Table 3.9: *Sprocket characteristics*

Driving gear	
Diamater	90 mm
Number of teeth	23
Driven gear	
Diameter	142 mm
Number of teeth	34

The gear ratio can be expressed simply as:

$$\tau = \frac{Z_{driven}}{Z_{driving}}$$

One positive effect given by the presence of this gear ratio is to make the braking module operate at higher torques than with a direct connection, thus reducing the presence of noise and interference on the torque values measured by the microcontroller.

Chapter 4

Activity description

The main objective of the activity is to analyze the response of the model to the presence of backlash on the transmission under different friction conditions. For this purpose, it is necessary to have a sufficiently large set of tests performed on the test bench in order to be able to verify the accuracy of the results proposed by the model.

4.1 Backlash selection and test

For the purpose of studying the behavior of the system subjected to backlash was necessary to firstly select different levels of backlash for testing. For this purpose, the range of human-appreciable backlash was identified and subdivided into 15 sampling stations, taking care to thicken them in the proximity of ”zero” backlash. The distribution of tests was organized in such a way in order to have greater resolution in the range where the backlash exhibits values close to possible operating conditions of EMA systems without, however, neglecting the borderline cases where any anomalous behavior result more easily observable.

Table 4.1: *Sampling points*

Sampling number	Micro-mover position [mm]	Theoretical backlash [rad]
1	14.00	0
2	13.80	1.153×10^{-3}
3	13.50	2.886×10^{-3}
4	13.30	4.043×10^{-3}
5	13.10	5.201×10^{-3}
6	12.80	6.942×10^{-3}
7	12.40	9.269×10^{-3}
8	12.00	1.160×10^{-2}
9	11.50	1.452×10^{-2}
10	11.00	1.746×10^{-2}
11	10.50	2.040×10^{-2}
12	10.00	2.335×10^{-2}
13	9.50	2.631×10^{-2}
14	9.15	2.839×10^{-2}
15	9.00	2.928×10^{-2}

The next step was to select the command under which to move the actuator. For this type of tests, a sinusoidal command of 7° amplitude and with a frequency of 0.2 Hz was therefore selected. The choice of this type of actuation was due to the fact that the sinusoidal command allows observation, during a single test, of the behavior of the system in the presence of backlash in both directions of movement. With regard to amplitude and frequency, such values were chosen so that the development of a reasonable segment where the actuator moves at a constant speed was possible in order to better observe the effects on the supplied currents.

A sample of the behavior of the bench during the tests is shown in the following figures.

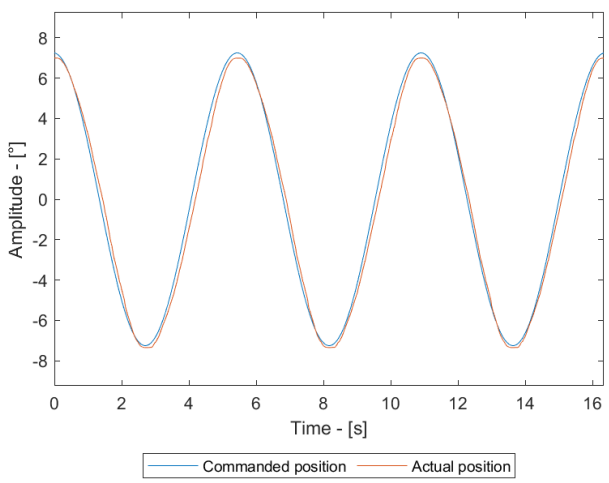

(a) *position*

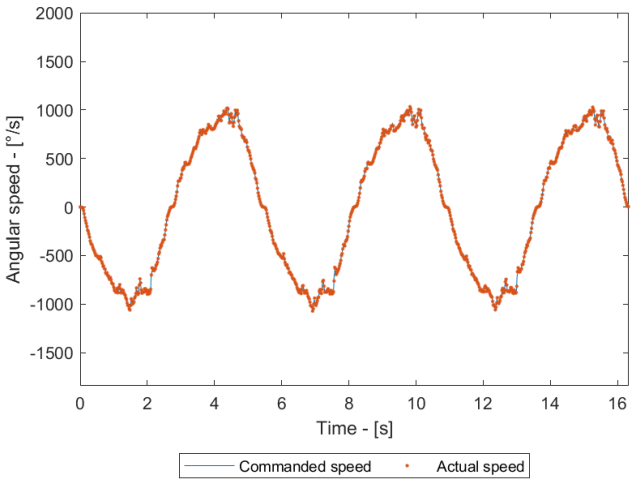

(b) *angular speed*

Figure 4.1: *Zero backlash (14.00* mm*) response*

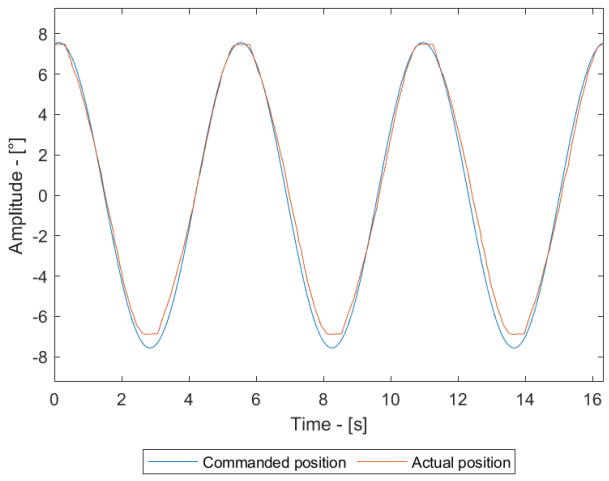

(a) *position*

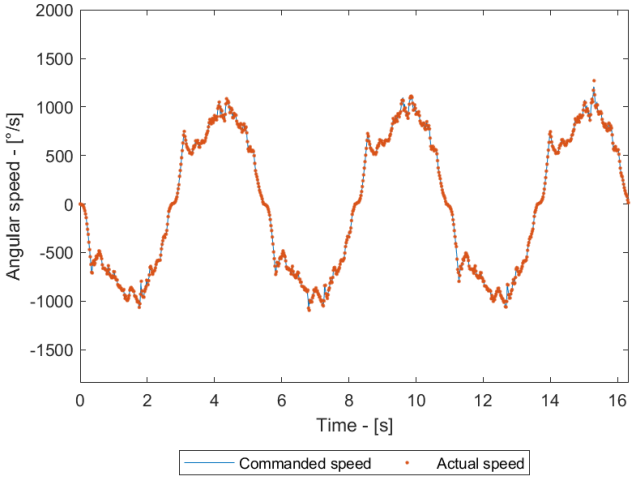

(b) *angular speed*

Figure 4.2: *Medium backlash (12.40* mm*) response*

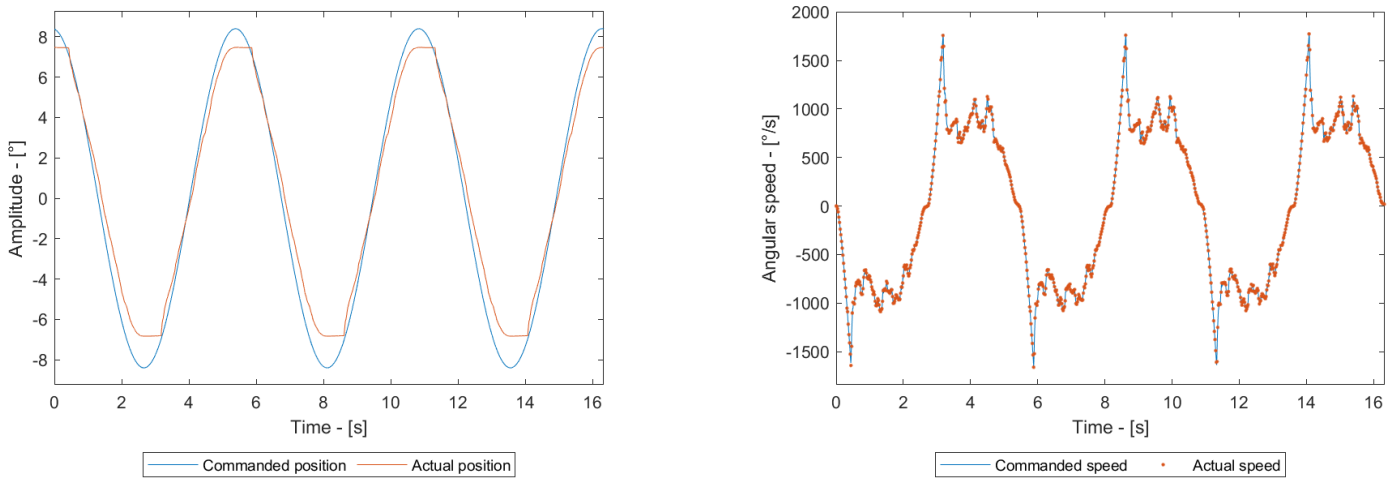

(a) *position* **(b)** *angular speed*

Figure 4.3: *High backlash (9.15* mm*) response*

4.2 Friction selection and test

In order to analyze the behavior of the system subjected to a combination of backlash and friction, it was at first necessary to select a subset of backlash at which to perform the tests. Three levels of play were selected for this purpose: no induced backlash, medium induced backlash and high induced backlash.

Selected the backlash levels, it was possible to move on to set the friction levels. The maximum resistive load was then imposed at 2 N m in order to keep motor operation point reasonably far from the S1 (60K) characteristic curve. The minimum friction level, on the other hand, was set at 0.9 N m so to introduce a resistance of such intensity so that it would be greater than the nominal friction of the entire transmission.

Table 4.2: *Sampling points*

Sampling number	Micro-mover position [mm]	Theoretical backlash [rad]	Friction command [Nm]
1	14.00	0	0.900
2			1.175
3			1.450
4			1.725
5			2.000
6	11.00	1.746×10^{-2}	0.900
7			1.175
8			1.450
9			1.725
10			2.000
11	10.00	2.335×10^{-2}	0.900
12			1.175
13			1.450
14			1.725
15			2.000

Similar to the frictionless tests, it was chosen to operate the motor with a sinusoidal command, but with a variation in amplitude and frequency settings. In this series of tests, it was indeed chosen to operate with an amplitude of 45° and a frequency of 0.05 Hz. These values were chosen in such a way to further widen the constant speed section and at the same time reduce the value of the actuation speed. The choice to decrease the actuation speed was made in an effort to relieve the thermal load on the brake module and at the same time ease the task of the brake control system.

The behavior of the test bench subjected to these test conditions turns out to be as shown below.

4.2.1 No induced backlash

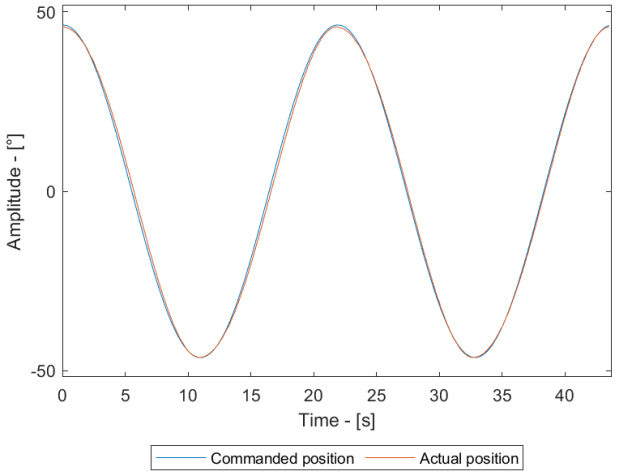

(a) *position*

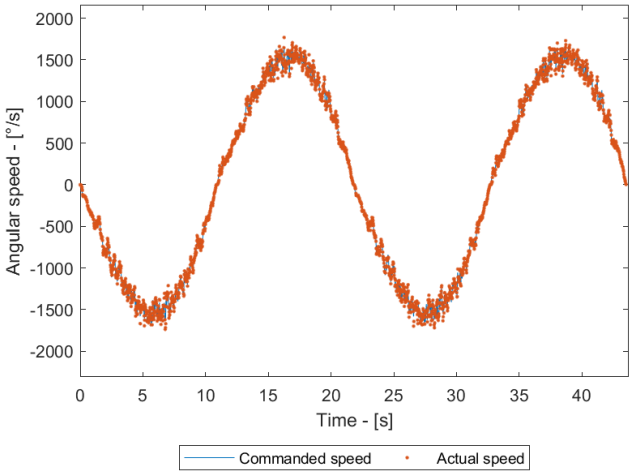

(b) *angular speed*

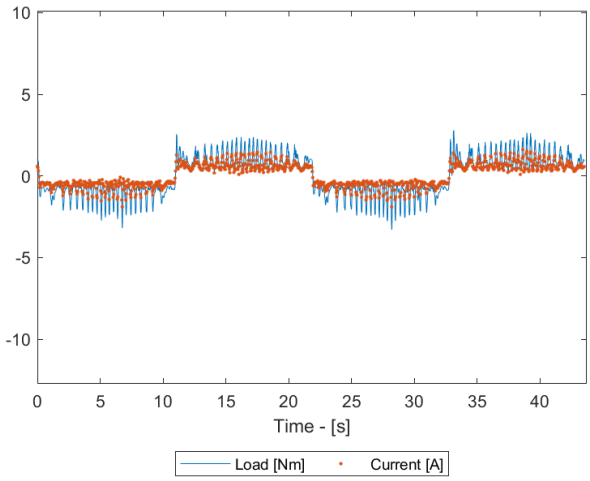

(c) *load and current*

Figure 4.4: Backlash = 14.00mm, friction = 0.900N m

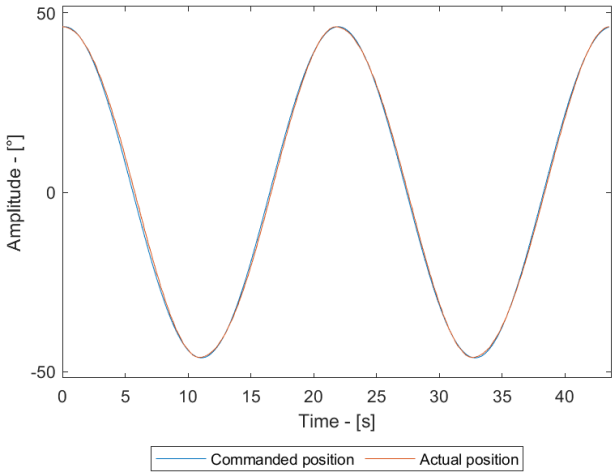

(a) *position*

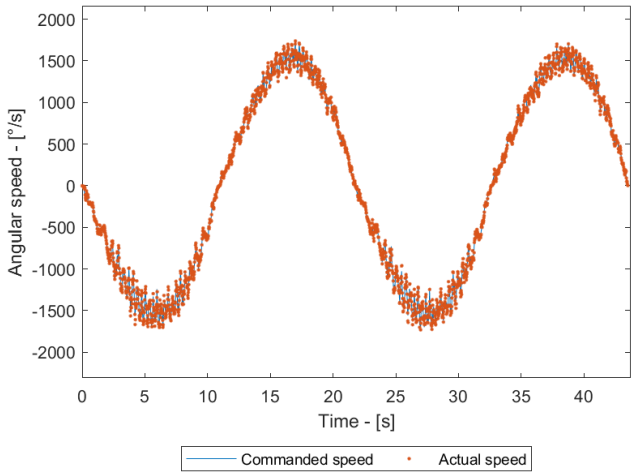

(b) *angular speed*

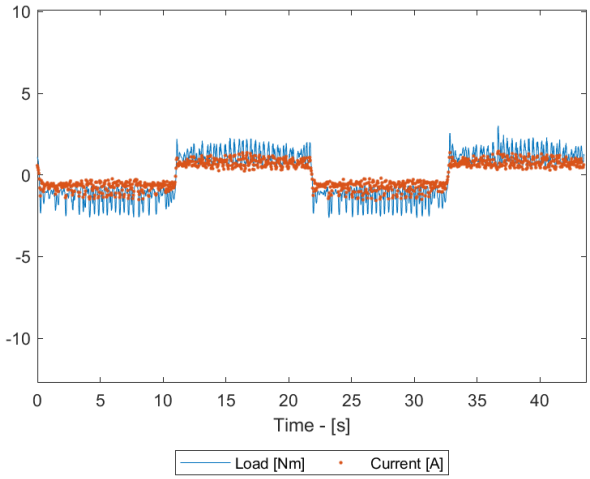

(c) *load and current*

Figure 4.5: Backlash = 14.00mm, friction = 1.175N m

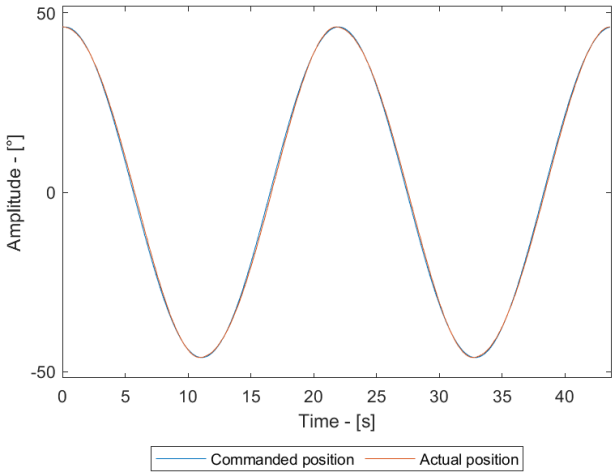

(a) *position*

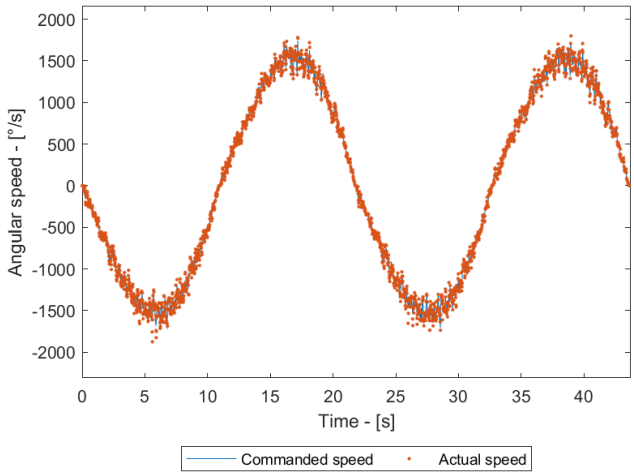

(b) *angular speed*

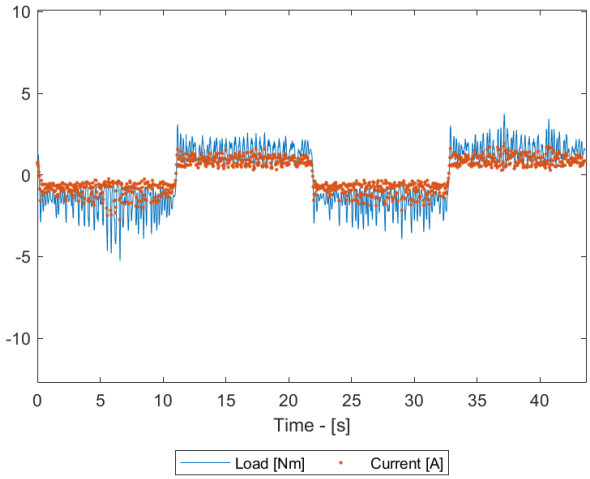

(c) *load and current*

Figure 4.6: Backlash = 14.00mm, friction = 1.450N m

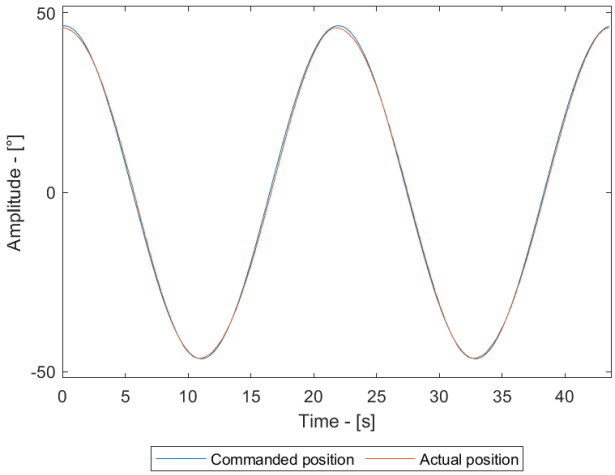

(a) *position*

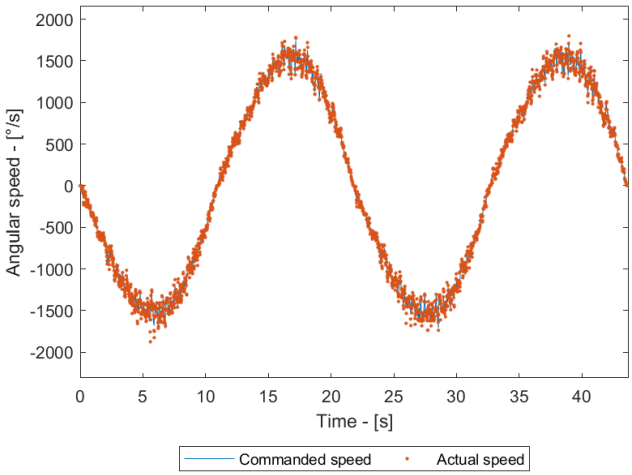

(b) *angular speed*

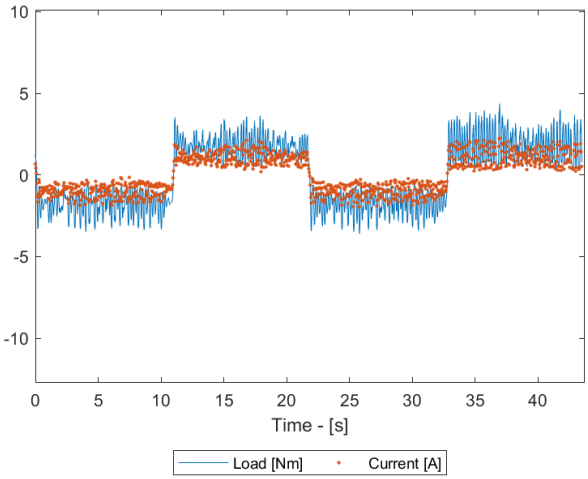

(c) *load and current*

Figure 4.7: Backlash = 14.00mm, friction = 1.725N m

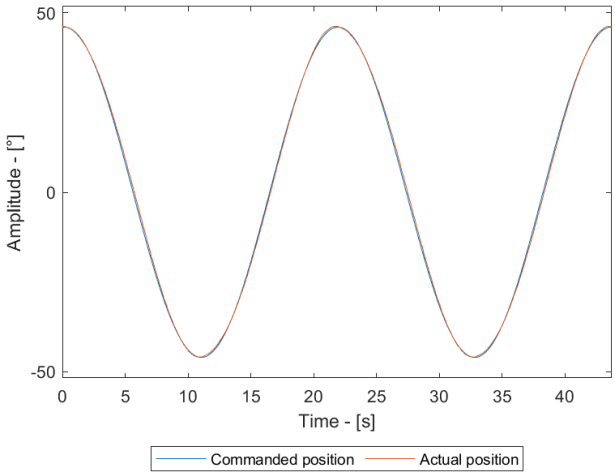

(a) *position*

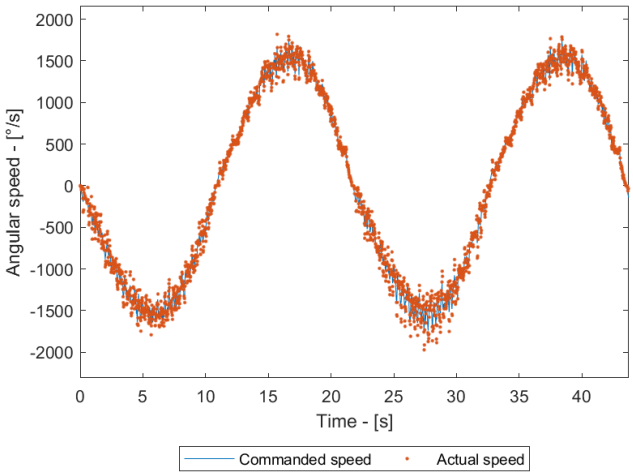

(b) *angular speed*

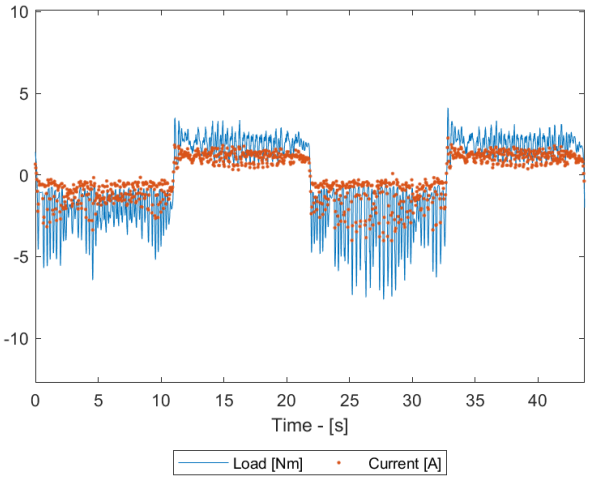

(c) *load and current*

Figure 4.8: Backlash = 14.00mm, friction = 2.000N m

4.2.2 Medium induced backlash

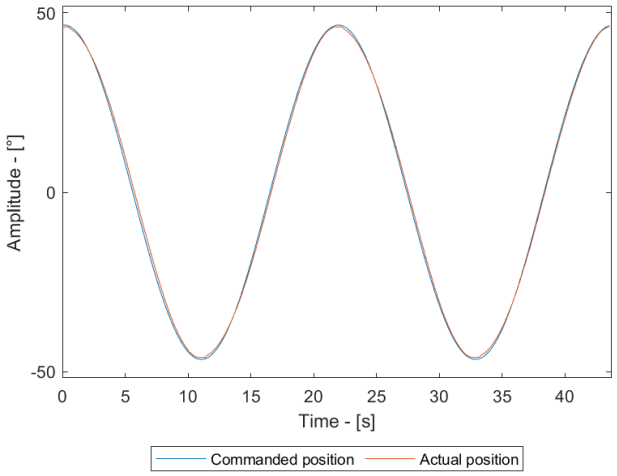

(a) *position*

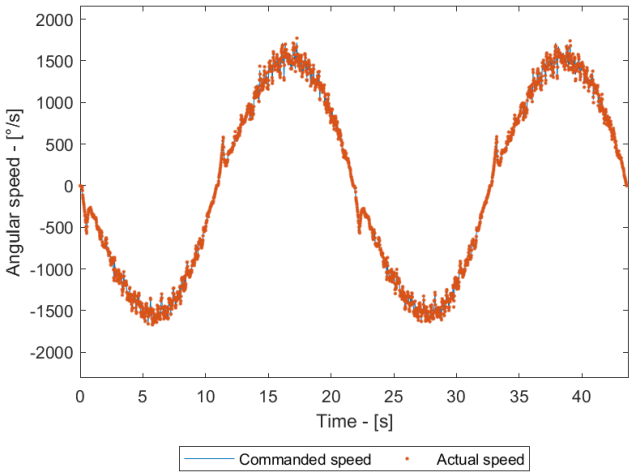

(b) *angular speed*

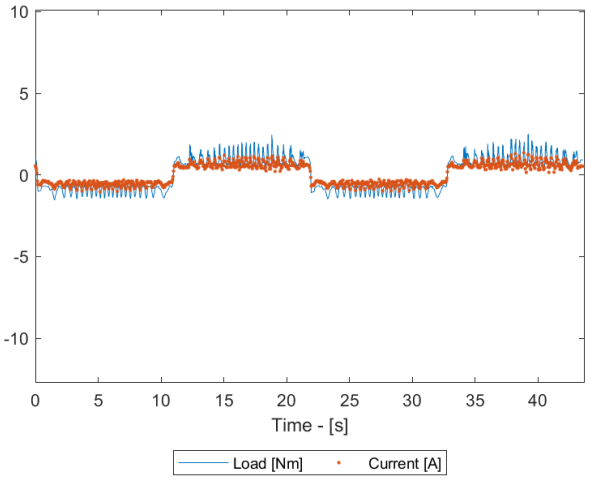

(c) *load and current*

Figure 4.9: Backlash = 11.00mm, friction = 0.900N m

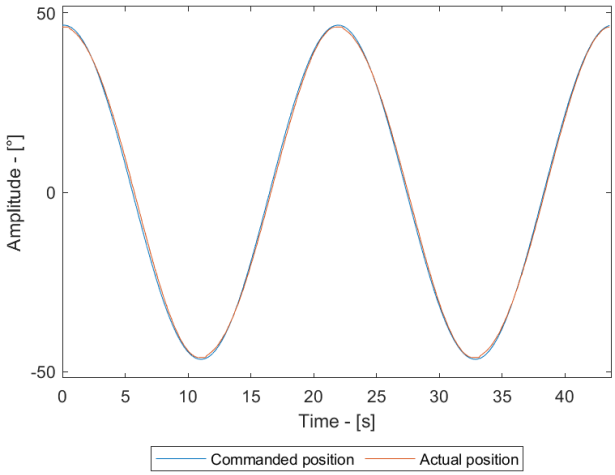

(a) *position*

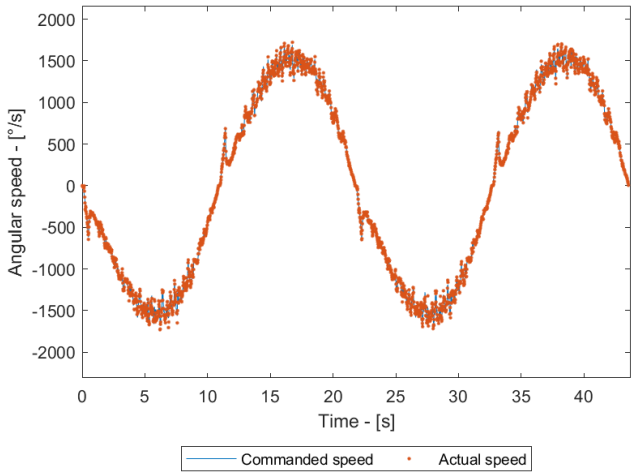

(b) *angular speed*

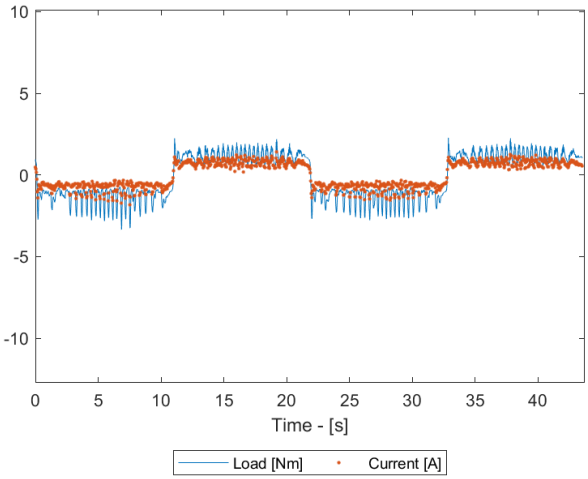

(c) *load and current*

Figure 4.10: Backlash = 11.00mm, friction = 1.175N m

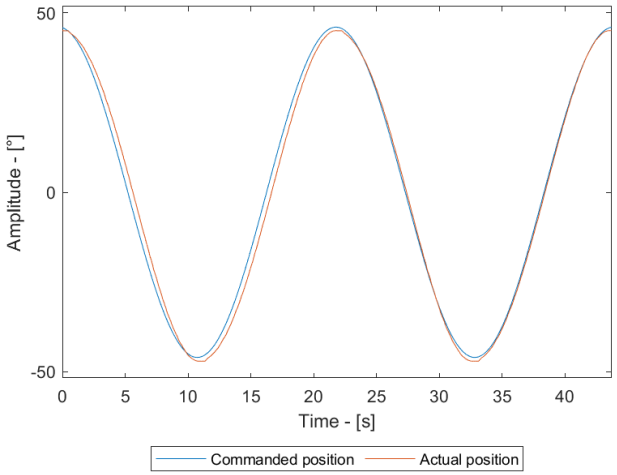

(a) *position*

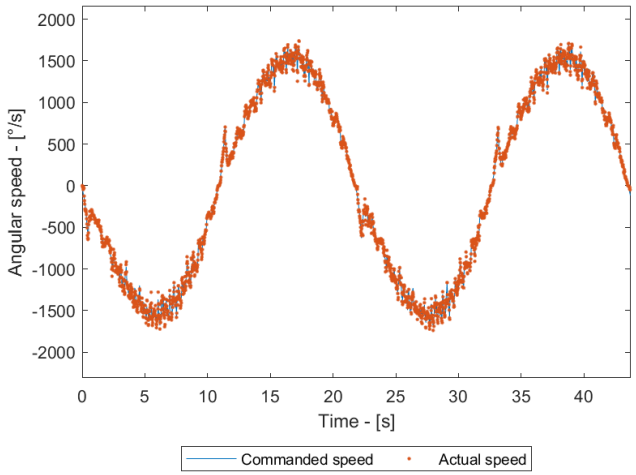

(b) *angular speed*

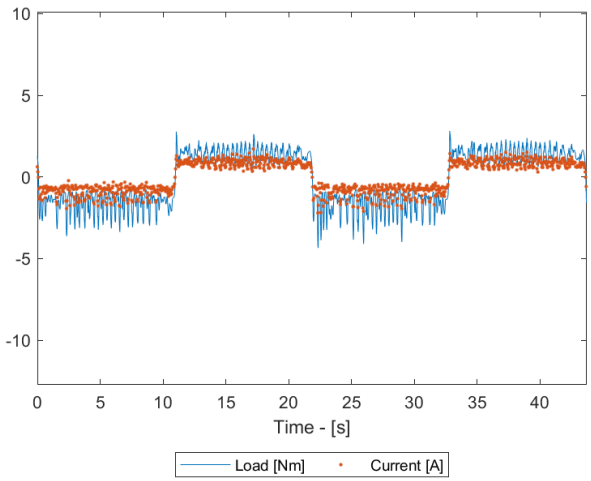

(c) *load and current*

Figure 4.11: Backlash = 11.00mm, friction = 1.450N m

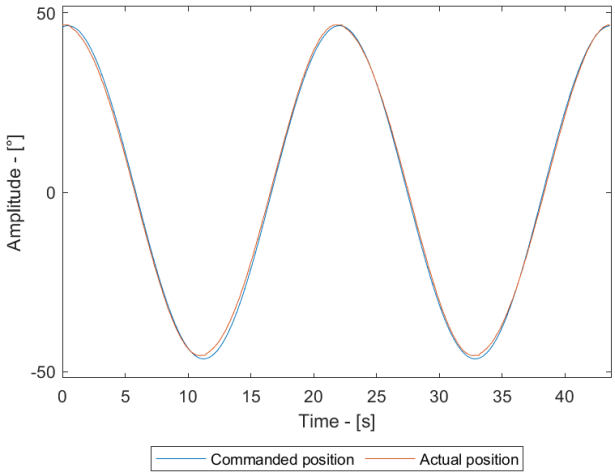

(a) *position*

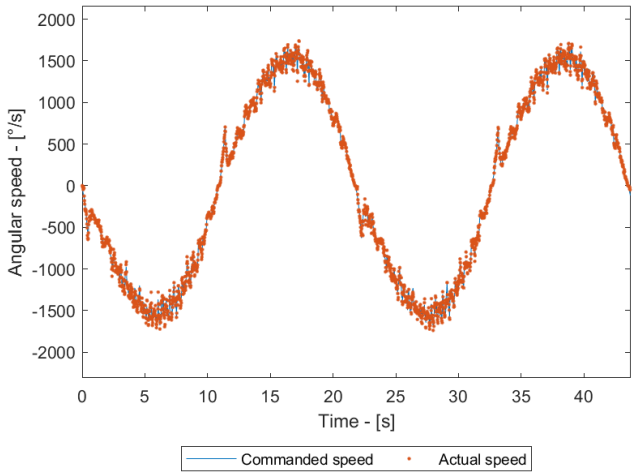

(b) *angular speed*

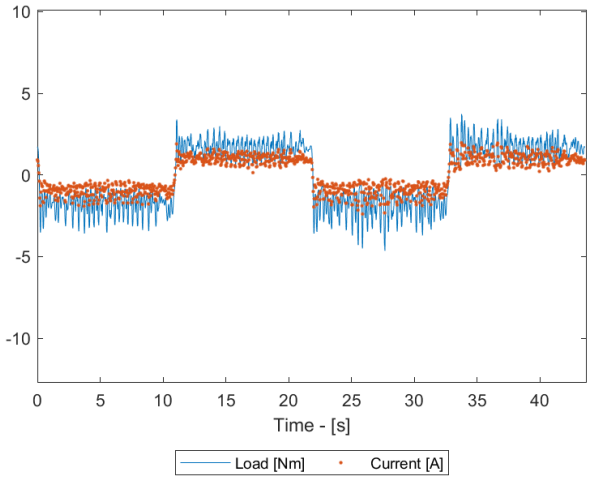

(c) *load and current*

Figure 4.12: Backlash = 11.00mm, friction = 1.725N m

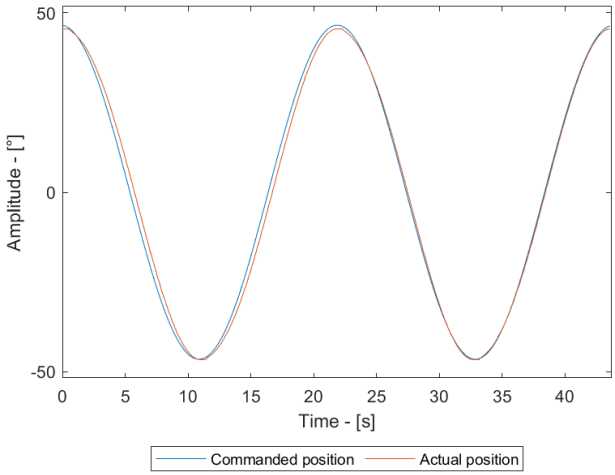

(a) *position*

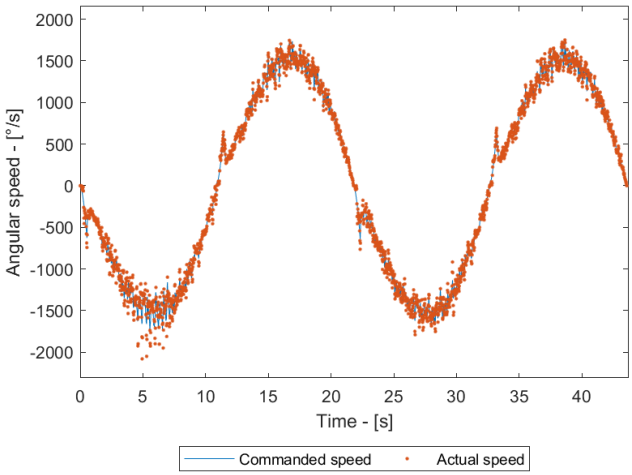

(b) *angular speed*

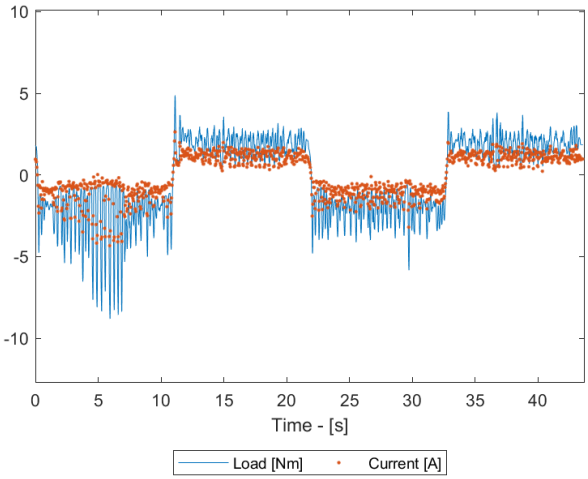

(c) *load and current*

Figure 4.13: Backlash = 11.00mm, friction = 2.000N m

4.2.3 High induced backlash

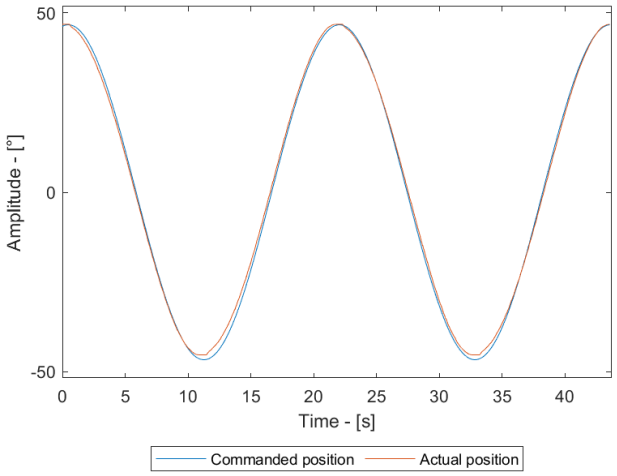

(a) *position*

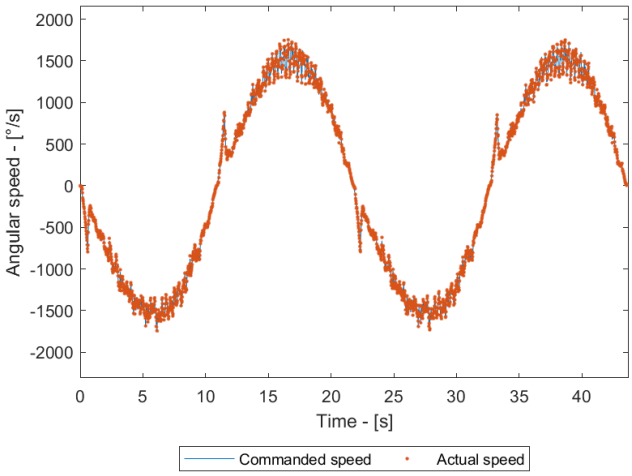

(b) *angular speed*

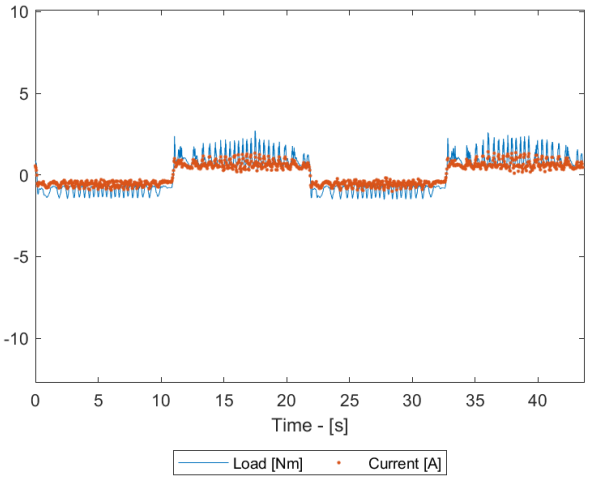

(c) *load and current*

Figure 4.14: Backlash = 10.00mm, friction = 0.900N m

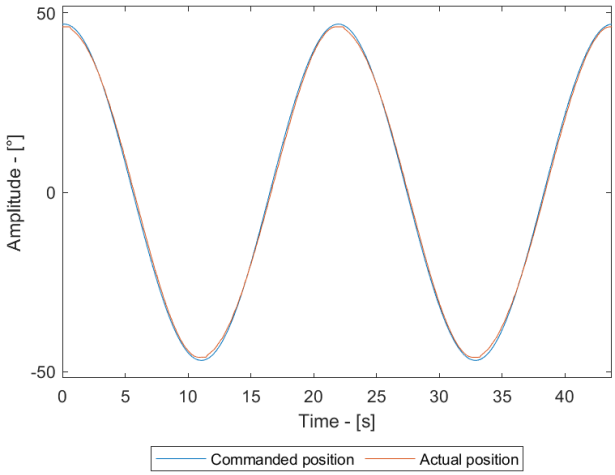

(a) *position*

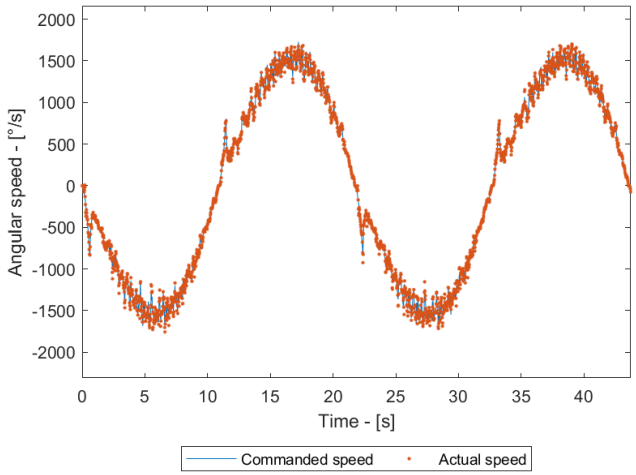

(b) *angular speed*

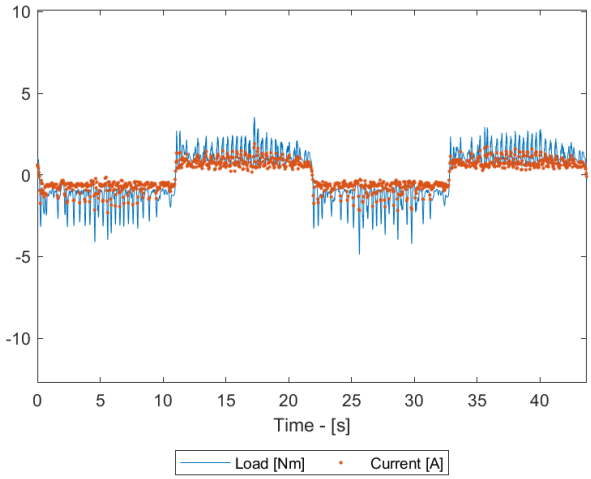

(c) *load and current*

Figure 4.15: Backlash = 10.00mm, friction = 1.175N m

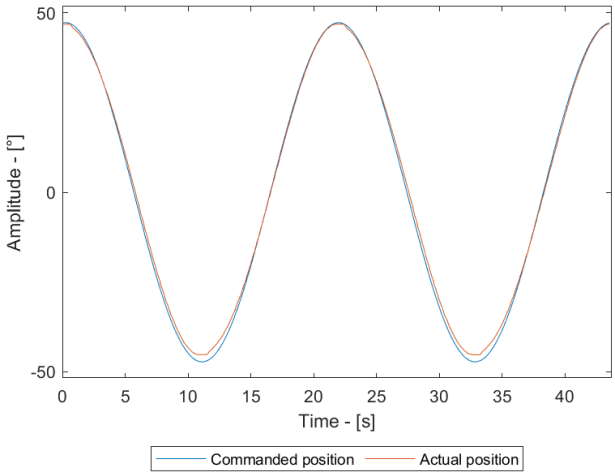

(a) *position*

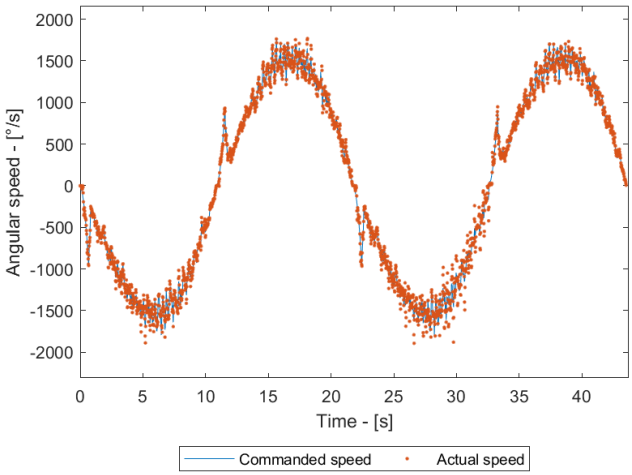

(b) *angular speed*

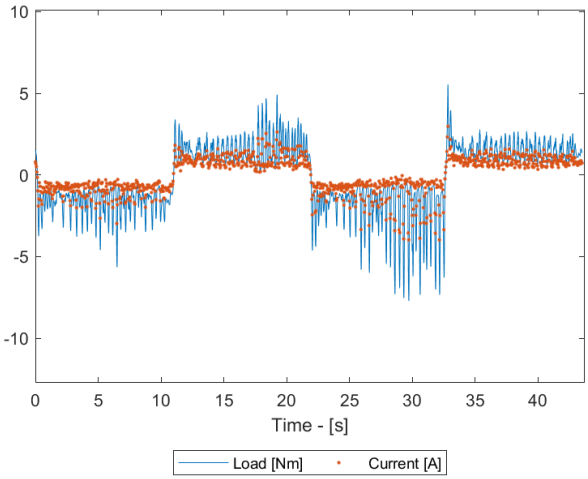

(c) *load and current*

Figure 4.16: Backlash = 10.00mm, friction = 1.450N m

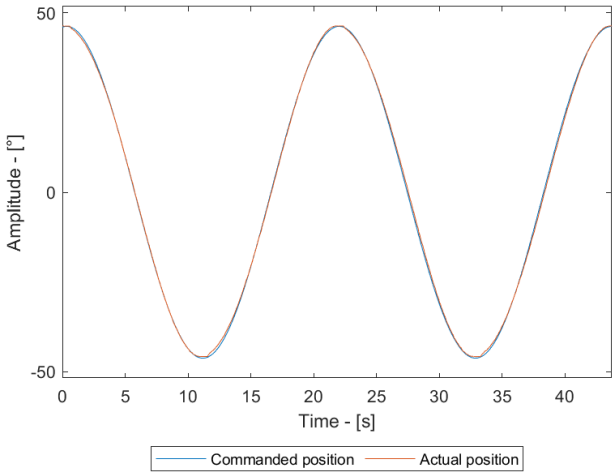

(a) *position*

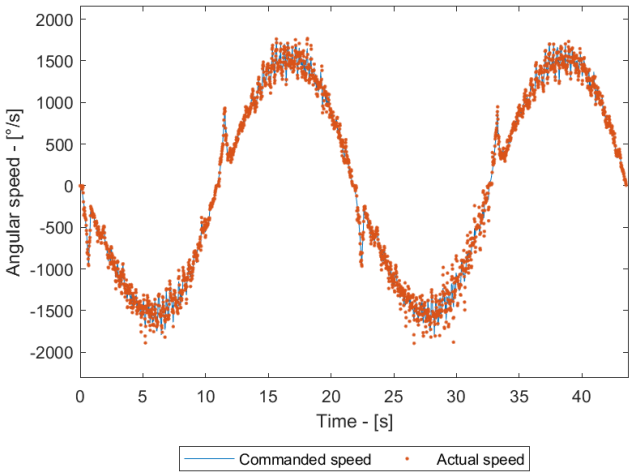

(b) *angular speed*

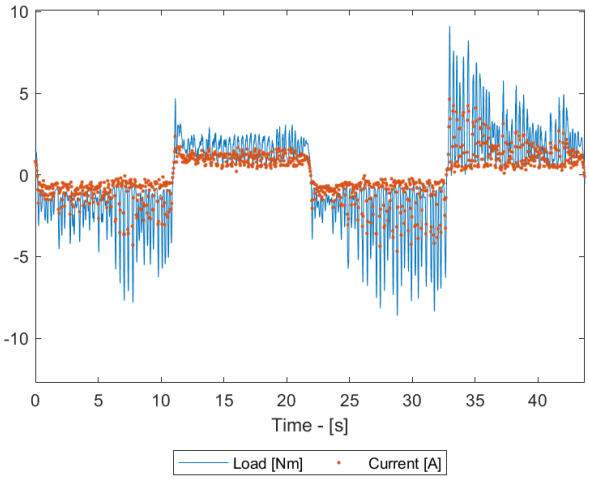

(c) *load and current*

Figure 4.17: Backlash = 10.00mm, friction = 1.725N m

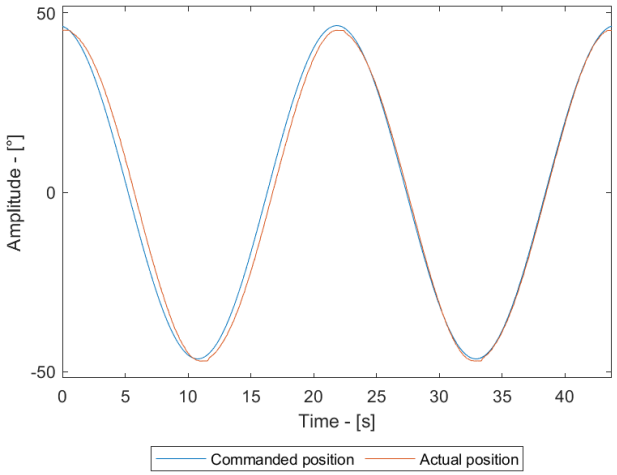

(a) *position*

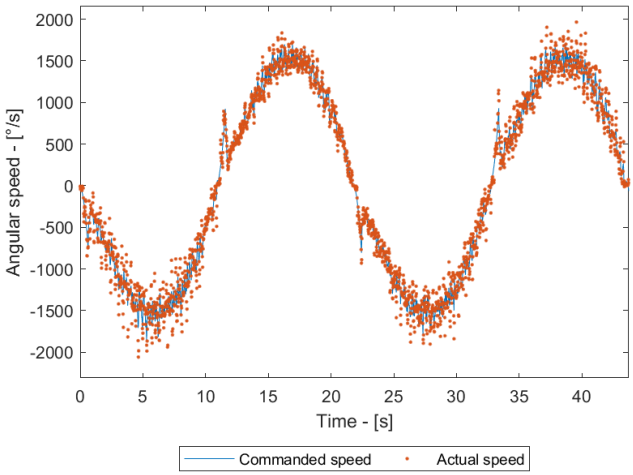

(b) *angular speed*

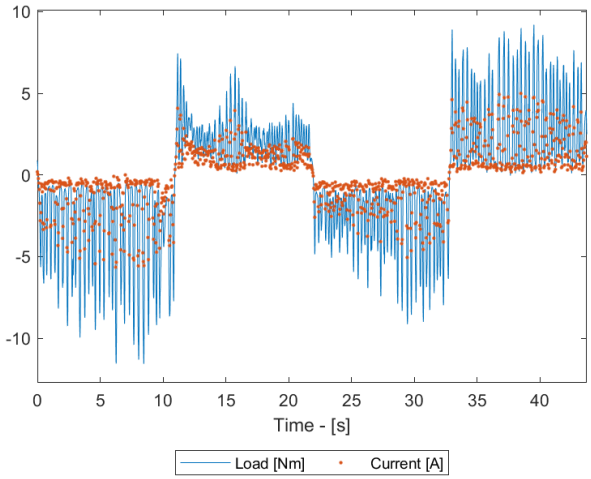

(c) *load and current*

Figure 4.18: Backlash = 10.00mm, friction = 2.000N m

4.3 Model parameters definition

In order to have all the parameters required for the execution of the model, it was necessary to determine the command actually imposed on the bench. To do this, a Fourier analysis of the position commanded by the PLC was used as a first step. This type of analysis made it possible to obtain the actual command

frequency, partially confirming the values of the characteristics imposed as a target. Once the frequency was established, it was possible to define the phase of the command signal. The determination of the phase was performed by minimizing the error between a pure sinusoidal signal and the generated command. By then resorting to a constrained optimization algorithm for nonlinear multi-variable functions, it was possible to define the initial phase and at the same time confirm the accuracy of the frequency derived in the previous step.

With all the necessary parameters well known, it was then possible to subject the model to the same operating conditions as the test bench.

Chapter 5

Results analysis

Obtained the experimental test data and reproduced the behavior of the model under the same operating conditions, it was possible to compare the different responses with the aim of verifying the precision of the model under analysis. The attention was therefore focused on five main aspects:

- discrepancies between theoretical and experimental backlash;
- ability of the model to faithfully reproduce the positional response of the experimental bench;
- ability of the model to replicate the actuation speeds of the test bench;
- ability to emulate the behavior of the currents;
- time required to reproduce the response of the real system.

5.1 Backlash in absence of external friction

The introduction of a movable carrier for the micro-mover leads to the need to characterize its operation. Therefore, the series of tests performed in the absence of friction allowed the experi-

mental backlash curve to be traced in order to compare the results with those predicted by the CAD model analysis.

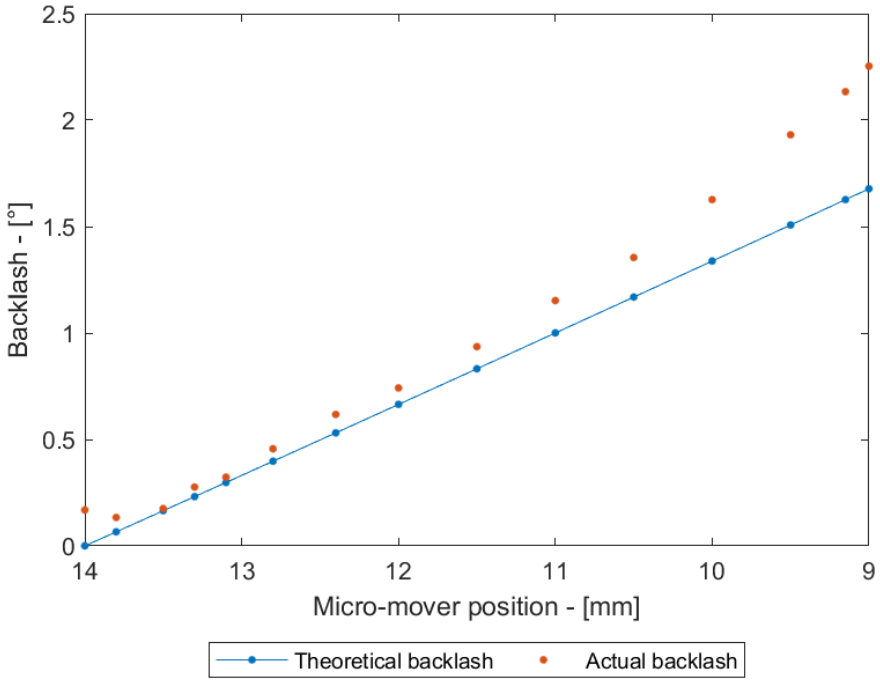

Figure 5.1: *Backlash in absence of external friction*

The Figure5.1 illustrates how the backlash values actually produced are similar to what had been estimated in the design phase. The discrepancies are in fact mainly due to the production techniques adopted for component development. In particular, the difficulty of most FDM systems to accurately reproduce curvilinear surfaces has led to the choice to use a circumference arc profile for the gear teeth. The arc profile, which is easier to reproduce, well approximates the ideal circumference involute but tends to deviate more precisely at the extreme positions of bottom and head of teeth. This explains the deviation for extreme micro-mover settings, conditions that cause the teeth to make contact at precisely these positions of greatest mismatch.

5.2 Position response in presence of external friction

Since the chosen commanding signal happens to be a position command the first variable to be analyzed was the position signal. The resulting test bench and model trends are as reported in the following figures.

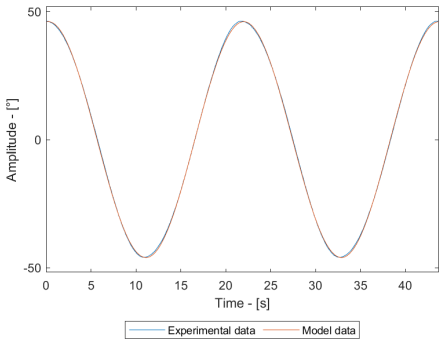

(a) backlash = 14.00mm

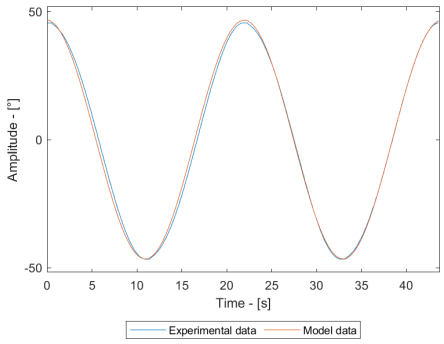

(b) backlash = 11.00mm

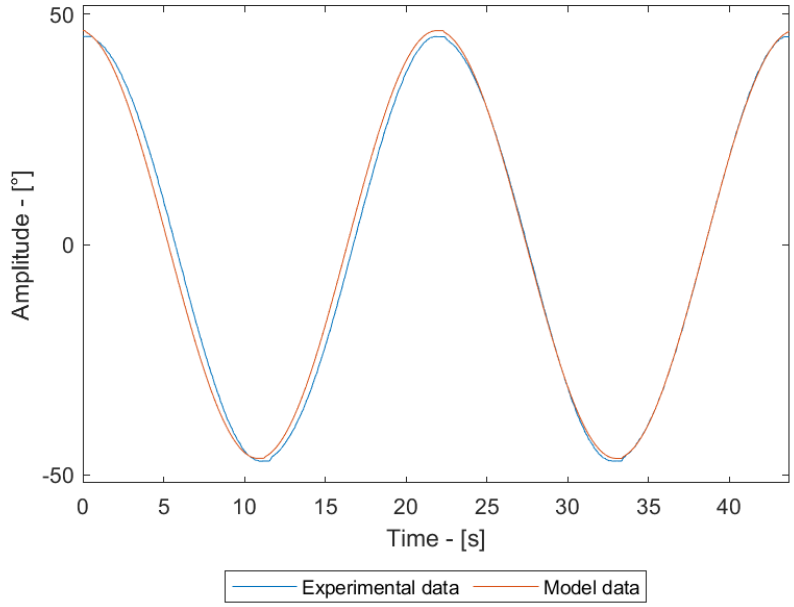

(c) backlash = 10.00mm

Figure 5.2: *Position at* friction = 2.000N m

From the above figures, it can be seen that even under the most critical conditions of maximum friction and maximum backlash, the model can accurately reproduce the behavior of the experimental bench. The model is in indeed able to capture backlash recovery with great accuracy, both in terms of amplitude and timing, as shown in Figure5.3; timing mismatch, in the worst case scenario, emerges to be roughly 0.346 s.

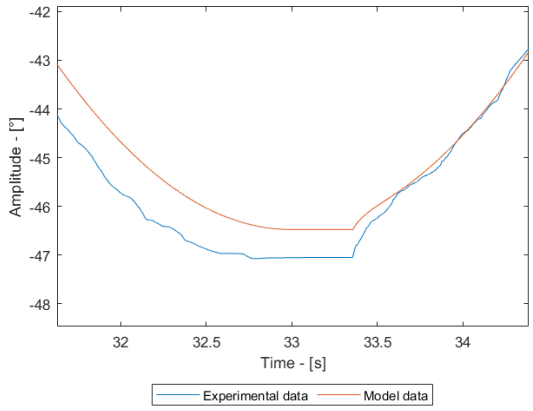

Figure 5.3: *Position detail at* friction = 2.000N m

In order to evaluate the precision and accuracy at the macroscopic level of the model and the effects of changes in friction and backlash, the mean square error (MSE) and standard error (SE) were used.

MSE is defined as:

$$\text{MSE} = \frac{1}{n}\sum_{i=1}^{n}(X_i - Y_i)^2$$

where:

- n = number of point
- X = observed value (test bench data)
- Y = predicted value (model data)

It thus defines a quantity that measures the dispersion of the predicted values around the experimental values that have been

obtained. Although it is a dimensional quantity, the most important aspect is its value: the smaller it is, the greater is the precision of the predictions delivered by the model.

The SE is a quantity that is often associated with the MSE. It allows to evaluate the average error that is committed by replacing the data predicted by the model with those actually observed on the bench. Its definition is as follows:

$$SE = \sqrt{\frac{s^2}{n}} = \sqrt{\frac{1}{n}\frac{1}{n-1}\sum_{i=1}^{n}(X_i - Y_i)^2} = \sqrt{\frac{1}{n-1}MSE}$$

where:

- s^2 = corrected sample variance

Thus, the MSE provides an overall estimation of the accuracy of the model while the SE provides a pin-point assessment of the proposed values by defining an error in dimensional terms.

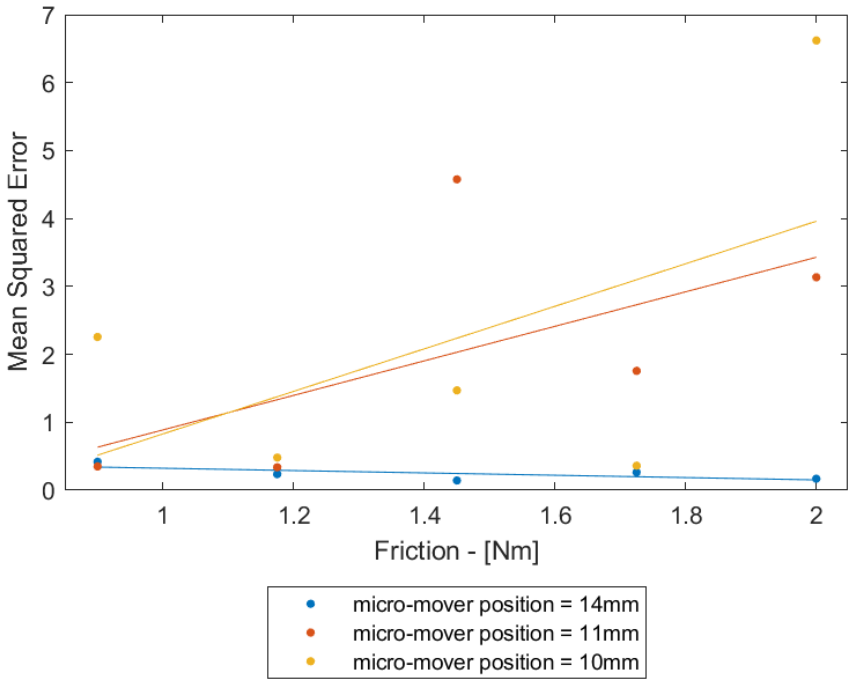

Figure 5.4: *Position Mean Squared Error*

Looking at the graphs in the Figure5.4 and Figure5.5, it is possible to see that, in the absence of external backlash, the effect of external friction is to increase the accuracy of the model. This phenomenon is probably due to the fact that the increase in friction leads to an increase in the actuated currents, thus making the effects produced by noise on the real system less noticeable and more comparable to what happen in the model.

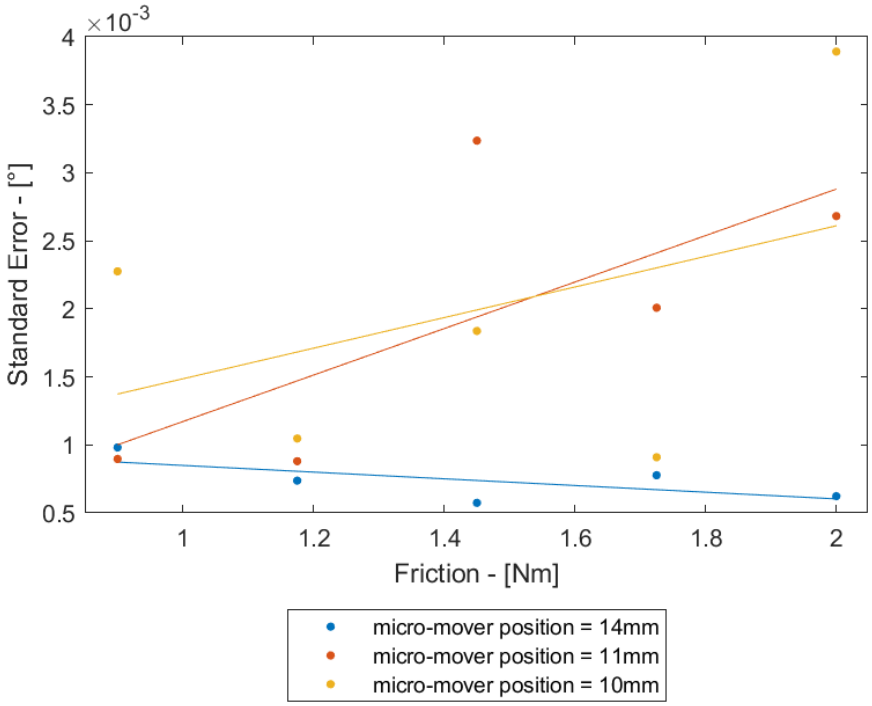

Figure 5.5: *Position Standard Error*

The results provided by the model exhibit a high degree of accuracy, in the worst case scenario, the SE does not exceed 0.008% of the position signal.

5.3 Speed response in presence of external friction

Analyzed the position, another important kinematic quantity is the angular speed. Comparing the response of the test bench and the model leads to the following graphs.

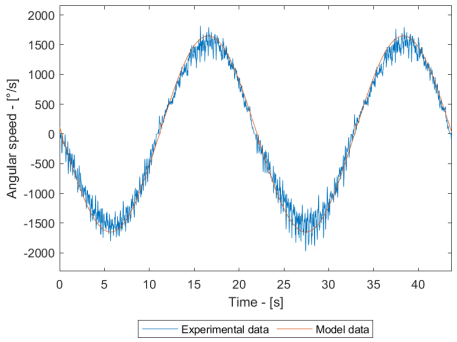

(a) backlash = 14.00mm

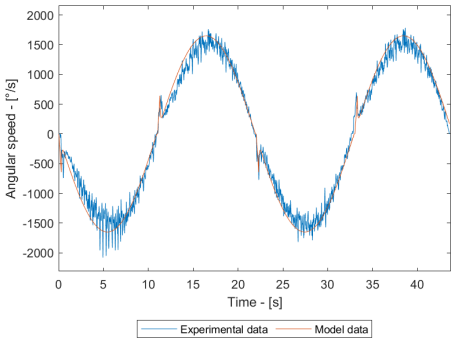

(b) backlash = 11.00mm

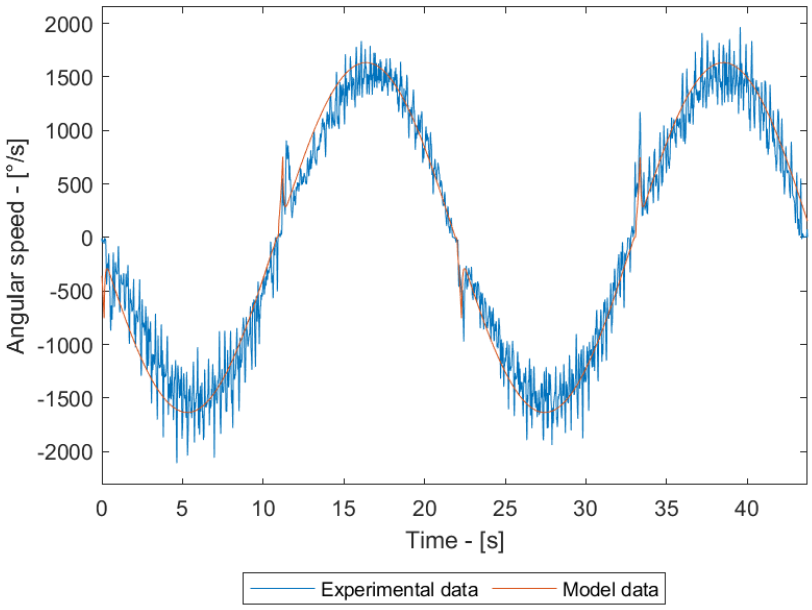

(c) backlash = 10.00mm

Figure 5.6: *Angular speed at* friction = 2.000N m

It is apparent from the preceding figures that the model under analysis reproduces the angular speed response of the experimental bench extremely accurately. It makes possible to predict the behavior of backlash recovery with an accuracy that appears to be very little affected by either the level of backlash present or the level of friction imposed.

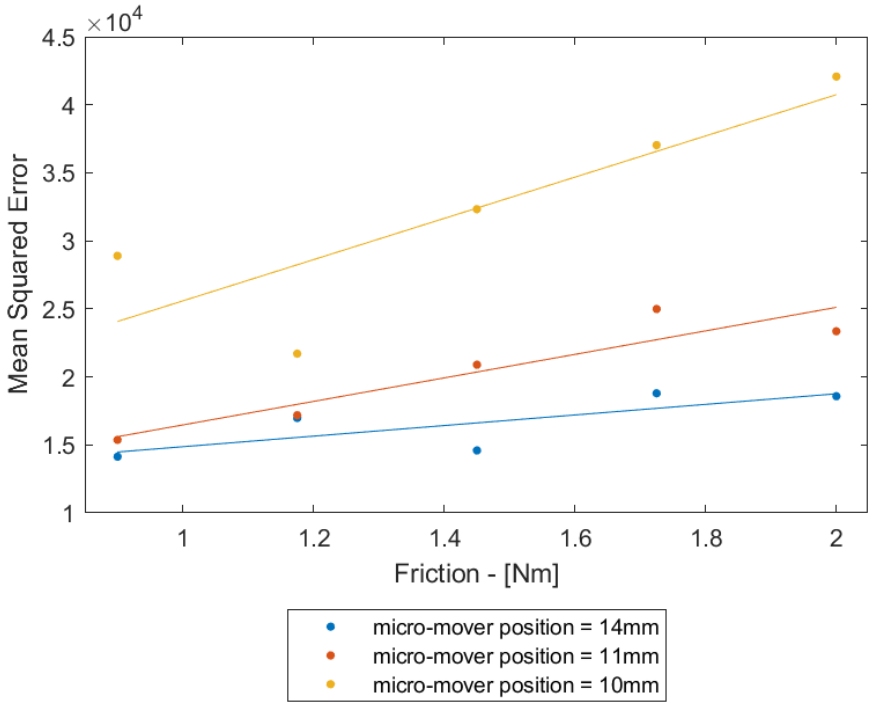

Figure 5.7: *Speed Mean Squared Error*

When examining the trends displayed in the graphs of Figure5.7 and Figure5.8 a linear-type correlation can be observed between resistive forces (friction) and model/bench discrepancies at all levels of backlash. The disposition of the curves, on the other hand, allow to state that the evolution of the errors as the backlash changes is not related to a linear type relationship; much of the evolution of the backlash occurs between the blue (backlash = 14.00mm) and red (backlash = 11.00mm) curves, and yet these curves are always closer compared to the red and yellow (backlash = 10.00mm) ones.

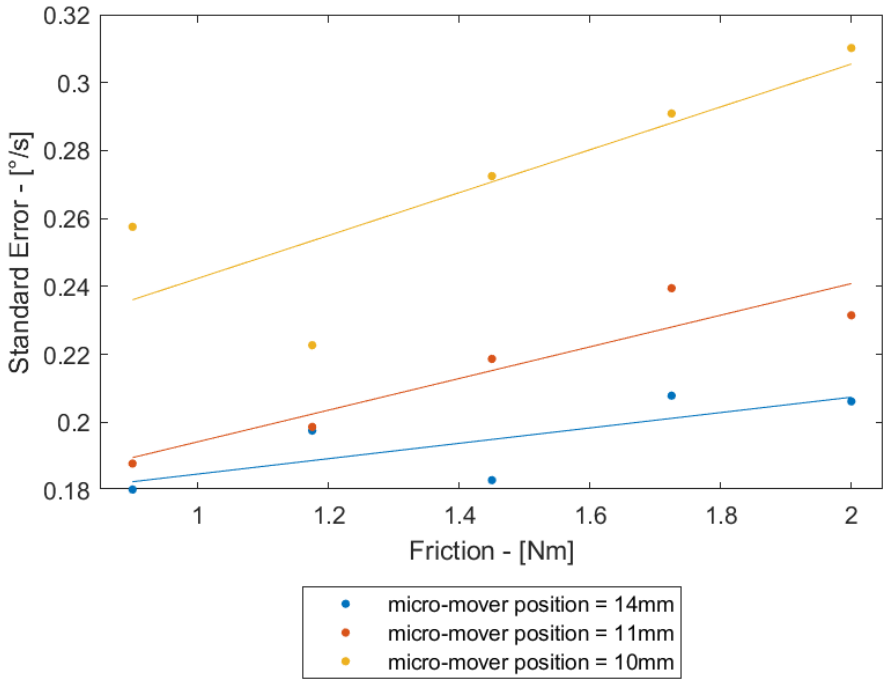

Figure 5.8: *Speed Standard Error*

The results provided by the model thus exhibit an even greater degree of accuracy than what was done for the position; in fact, the SE does not exceed 0.019% of the angular speed.

5.4 Current response in presence of external friction

Having analyzed the most significant kinematic variables, the electrical variable under investigation has been the current.

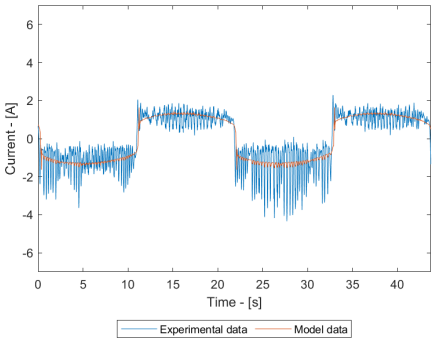

(a) backlash = 14.00mm

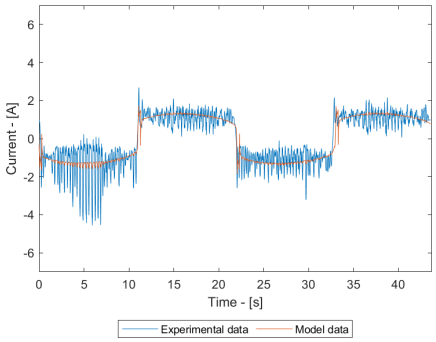

(b) backlash = 11.00mm

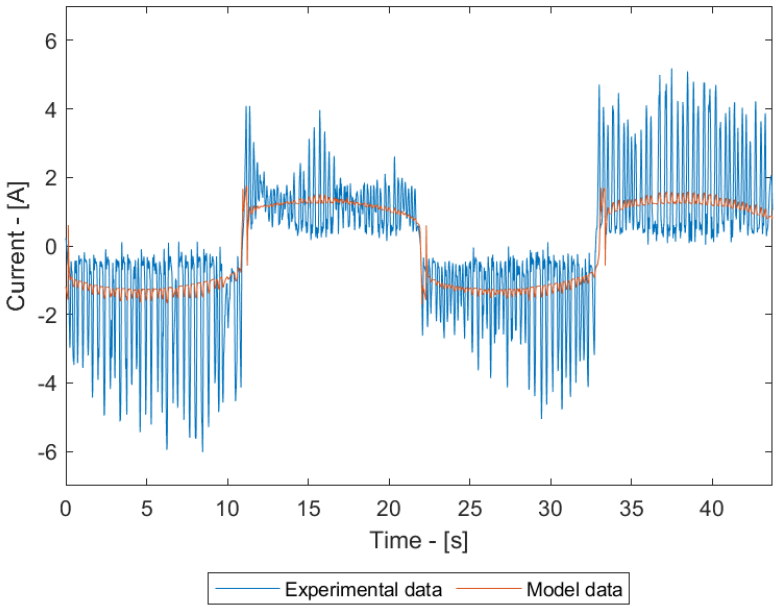

(c) backlash = 10.00mm

Figure 5.9: *Current at* friction = 2.000N m

By examining the evolution of the responses of the two systems as the level of backlash changes, it is possible to appreciate how well the numerical model captures the trend of what is measured on the bench.

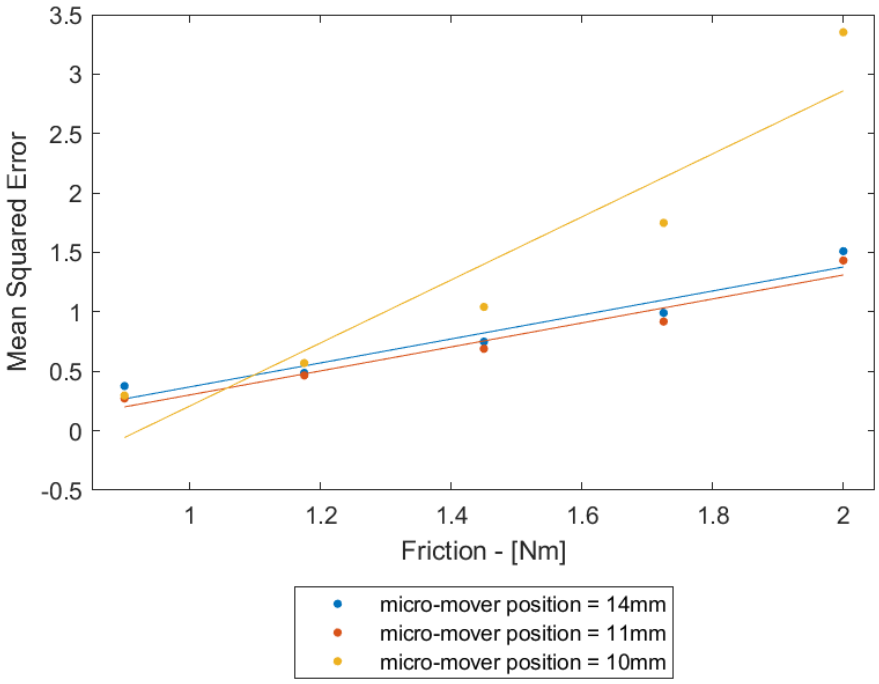

Figure 5.10: *Current Mean Squared Error*

In particular, analyzing the tendencies found in the graphs of Figure5.10 and Figure5.11, it is possible to appreciate how the degree of accuracy of the model remains largely unchanged as the backlash varies. The proximity of the blue (backlash = 14.00mm) and red (backlash = 11.00mm) curves also observed for angular speed is even more pronounced. The two curves appear in this case to be nearly parallel and separated at most by 0.1 mA (value obtained for the SE graph). The trend in the amount of error present in the results produced by the model deviates from those obtained in the absence of backlash only for values so high that they are close to conditions that can cause the encoder to lose complete contact with the gearbox.

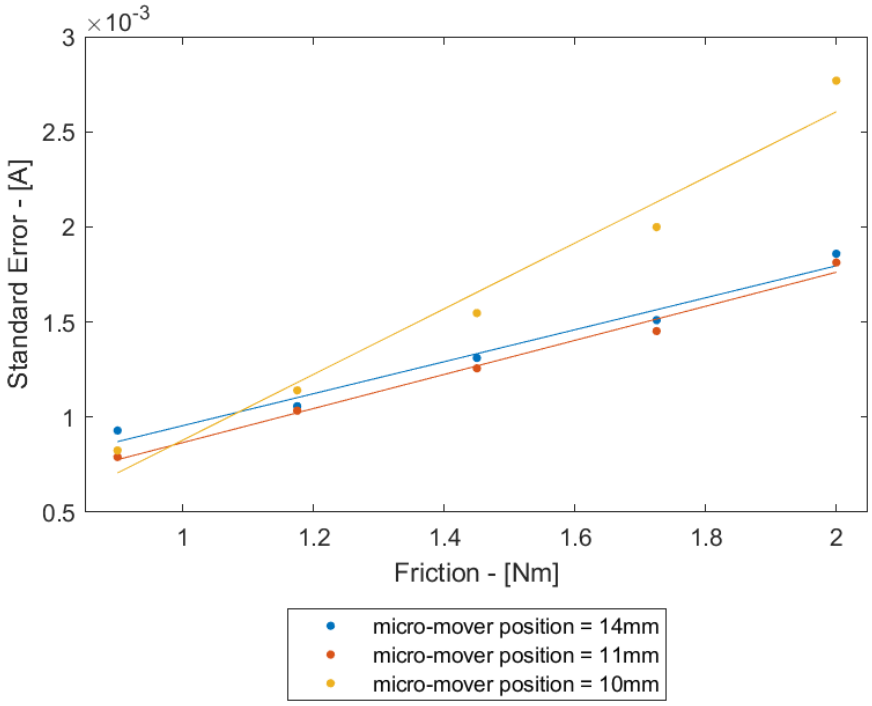

Figure 5.11: *Current Standard Error*

The model thus provides an approximation of the behavior of the real system with an error that, in the worst case, does not exceed 0.157% of the actual value.

5.5 Simulation time

Given the sensible number of simulations performed with the model, it became possible to assess its computational complexity. The following adimensional quantity has been selected for the definition of the complexity:

$$c = \frac{t_{model}}{t_{bench}}$$

By then averaging over all the tests the resulting variable it is possible to achieve a single value characterizing the computational complexity of the entire model. This operation leads to the result that 17.452$\pm$0.562 seconds of simulation are required for

every single second of data collection taken on the bench. Such a result is due to the particularly short integration step required by the portion of the model that reproduces the electrical behavior of the bench. The small integration step make inevitable to compute a large number of points resulting in increased computation time.

Chapter 6

Conclusions and future developments

The series of tests performed in the presence of an external load (which represents the internal friction within the gearbox) at different degrees of backlash provided a database that can be used to validate the described model. The subsequent analysis showed, therefore, how the proposed model is able to reproduce the behavior of the test bench with a high degree of accuracy.

The model that was considered, while able to provide a high level of accuracy, suffers from a significant computational cost and consequent simulation time. Therefore, it would be possible to use the database developed here to verify alternative models designed with the goal of reducing complexity and simulation time.

Looking at the experimental apparatus, it is possible to notice that the control system for the braking force is not perfectly able to exert an accurate command. The mean value produced corresponds to the desired value but the oscillations can also be of considerable intensity. It would therefore be possible to investigate alternative control techniques, such as a fit-forward archi-

tecture, in order to reduce the oscillations and prevent the different components from approaching the limit values of torque and current. Another point of interest proves to concern the recreation of the effects of load on the entire system with the potential to equip the transmission with sensors.

Bibliography

[1] J. Li, Z. Yu, Y. Huang, and Z. Li, "A review of electromechanical actuation system for more electric aircraft," in *2016 IEEE International Conference on Aircraft Utility Systems (AUS)*, pp. 490–497, IEEE, 2016.

[2] M. E. Roth, L. M. Taylor, and I. G. Hansen, "Status of electrical actuator applications," in *IECEC 96. Proceedings of the 31st Intersociety Energy Conversion Engineering Conference*, vol. 1, pp. 191–196, IEEE, 1996.

[3] K. Goebel, G. Vachtsevanos, and M. E. Orchard, "Prognostics," tech. rep., SAE, 2013.

[4] G. Qiao, G. Liu, Z. Shi, Y. Wang, S. Ma, and T. C. Lim, "A review of electromechanical actuators for more/all electric aircraft systems," *Proceedings of the Institution of Mechanical Engineers, Part C: Journal of Mechanical Engineering Science*, vol. 232, no. 22, pp. 4128–4151, 2018.

[5] J. Luo, M. Namburu, K. Pattipati, L. Qiao, M. Kawamoto, and S. Chigusa, "Model-based prognostic techniques [maintenance applications]," in *Proceedings AUTOTESTCON 2003. IEEE Systems Readiness Technology Conference.*, pp. 330–340, Ieee, 2003.

[6] P. C. Berri, M. D. Dalla Vedova, P. Maggiore, and G. Riva, "Design and development of a planetary gearbox for electromechanical actuator test bench through additive man-

ufacturing," in *Actuators*, vol. 9, p. 35, MDPI, 2020.

[7] G. Jacazio and S. Pastorelli, *Meccanica applicata alle macchine*. Levrotto & Bella, 2001.

[8] F. Mecatti, *Statistica di base. Come, quando e perché*. McGraw-Hill, 2010.

[9] P. Sciandra, "Development and experimental validation of prognostic algorithms for electromechanical actuators," 2020.

[10] V. Boschetti, "Development of an experimental test bench for the validation of prognostic algorithms for electromechanical actuators," 2020.

[11] P. Maggiore, "Modellazione, simulazione e sperimentazione dei sistemi aerospaziali." University Lecture.

[12] P. Maggiore, "Sistemi di bordo aerospaziali." University Lecture.

[13] Siemens, *Data sheet for SIMOTICS S-1FK7*.

[14] Siemens, *SIMOTICS S-1FK7 motor characteristics*.

[15] Siemens, *Data sheet for SINAMICS Power module PM240-2*.

[16] Siemens, *SIMATIC IPC427E Product Information*.

[17] Siemens, *Data sheet for SINAMICS S120 control unit CU310-2 PN*.

[18] Italsensor, *Incremental optical encoders TSW58HS*.